Lactoferrin binding to Sars-CoV-2 Spike glycoprotein protects host from infection, inflammation and iron dysregulation.

Antimo Cutone
University of Molise Department of Bioscience and Environment: Universita degli Studi del Molise Dipartimento di Bioscienze e Territorio
Luigi Rosa
Sapienza University of Rome Department of Public Health and Infectious Diseases
Maria Carmela Bonaccorsi di Patti
Sapienza University of Rome Department of Biochemical Sciences
Federico Iacovelli
Univ of Rome Tor Vergata Department of Biologyersity
Maria Pia Conte
Sapienza University of Rome Department of Public Health and Infectious Diseases
Giusi Ianiro
University of Molise Department of Bioscience and Territory: Universita degli Studi del Molise Dipartimento di Bioscienze e Territorio
Alice Romeo
University of Rome Tor Vergata Department of Biology
Elena Campione
University of Rome Tor Vergata Dermatology Unit
Luca Bianchi
University of Rome Tor Vergata Dermatology Unit
Piera Valenti
Sapienza University of Rome Department of Public Health and Infectious Diseases
Mattia Falconi
University of Rome Tor Vergata Department of Biology
Giovanni Musci (musci@unimol.it)
University of Molise Department of Bioscience and Territory: Universita degli Studi del Molise Dipartimento di Bioscienze e Territorio https://orcid.org/0000-0002-5196-709X

Research Article

Keywords: Lactoferrin, SARS-CoV-2, COVID-19, Iron homeostasis, Inflammation

Posted Date: May 17th, 2022

DOI: https://doi.org/10.21203/rs.3.rs-1605740/v1

Lactoferrin binding to Sars-CoV-2 Spike glycoprotein protects host from infection, inflammation and iron dysregulation.

Antimo Cutone[1*], Luigi Rosa[2*], Maria Carmela Bonaccorsi di Patti[3], Federico Iacovelli[4], Maria Pia Conte[2], Giusi Ianiro[1], Alice Romeo[4], Elena Campione[5], Luca Bianchi[5], Piera Valenti[2], Mattia Falconi[4] and Giovanni Musci[1#]

[1] Department of Biosciences and Territory, University of Molise, Pesche, Italy.

[2] Department of Public Health and Infectious Diseases, Sapienza University of Rome, Italy.

[3] Department of Biochemical Sciences, Sapienza University of Rome, Italy.

[4] Department of Biology, University of Rome "Tor Vergata", Rome, Italy.

[5] Dermatology Unit, University of Rome "Tor Vergata", Rome, Italy.

[*]These authors equally contributed to the manuscript

[#]Corresponding author: Giovanni Musci (musci@unimol.it).

Keywords: Lactoferrin, SARS-CoV-2, COVID-19, Iron homeostasis, Inflammation

Abstract

The anti-SARS-Cov-2 activity of the iron-binding protein Lactoferrrin has been investigated in epithelial and macrophagic cell models using a Pseudovirus decorated with the SARS-CoV-2 Spike glycoprotein. The human and, even more, the nutraceutically available bovine Lactoferrin inhibit pseudoviral infection in all cellular models tested. The bovine protein efficiently counteracts the deleterious effects of purified Spike on iron and inflammatory homeostasis, as shown by restored levels of the main proteins of the iron-handling system and, in the case of macrophagic THP-1 cells, of the proinflammatory cytokines IL-1β and IL-6. A direct interaction between Lactoferrin and Spike is likely at the basis of the observed effects, as demonstrated by an in vitro pull-down assay. Finally, *in silico* approaches have been applied to analyze the interactions of human and bovine Lactoferrins with Transferrin Receptor 1, a potential gate for SARS-CoV-2 entry into cells, as well as the binding of the bovine protein to different variants of concern of the SARS-Cov-2 Spike glycoprotein. Our results give hope for the employment of bovine Lactoferrin as an adjuvant of the standard of care therapies in COVID-19 treatment.

Introduction

Severe acute respiratory syndrome coronavirus 2 (SARS-CoV-2), the causative agent of coronavirus disease (COVID)-19, is an enveloped, positive-sense, single-stranded RNA betacoronavirus possessing about 79% identity to SARS-CoV [1]. SARS-CoV-2 has four major structural proteins, namely nucleocapsid, membrane, envelope and Spike [1]. The first critical step of viral infection is catalyzed by its trimeric Spike glycoproteins, which decorate the virion surface. Spike binds to angiotensin-converting enzyme 2 (ACE2) through its receptor binding domain (RBD) within the S1 subunit, triggering proteolytic cleavage of Spike, fusion of the S2 subunit with the host cell membrane [2] and endocytosis of the viral particle [3]. In addition, the negative charges of cellular heparan sulfate proteoglycans (HSPGs) electrostatically interact with basic residues of Spike and strongly contribute to the early interaction between SARS-CoV-2 and host cells [2].

The pathology of SARS-CoV-2 is further worsened by the activation of innate immune cells and the release of inflammatory cytokines aimed at counteracting the viral infection. Activation of the immune response is essential for antiviral host defense, but an excessive release of proinflammatory cytokines, such as interleukin (IL)-6, could result in tissue injury, systemic inflammation and organ failure [4]. In this regard, Spike is involved in the massive release of pro-inflammatory cytokines [5]. In particular, Spike (both from SARS-CoV and SARS-CoV-2) is a potent viral pathogen-associated molecular pattern (PAMP) sensed by toll-like receptor 2 (TLR2), which activates the NF-κB pathway, leading to the expression of inflammatory mediators in innate immune and epithelial cells [5]. However, the detailed mechanism(s) of the hyperinflammatory response during SARS-CoV-2 infection are still poorly understood.

Proinflammatory cytokines, particularly IL-6, can markedly influence iron homeostasis [6]. Systemic iron homeostasis is tightly controlled in humans. Both iron acquisition by enterocytes and iron recycling by macrophages are regulated through iron absorption, storage, and export, as mammals lack a direct iron excretion system [7].

Dietary iron enters the body at the duodenal level through the concerted action of the ferrireductase DCYTB and the metal importer DMT-1 [8]. Enterocytes then release iron in the plasma through ferroportin (Fpn), the only iron exporter identified so far in mammalian cells [9]. Either one of two ferroxidases: hephaestin, mainly expressed by small intestine, and ceruloplasmin (Cp), which is synthesized by hepatocytes, macrophages, and immune cells [10], is required to convert the exported ferrous iron into its ferric form to allow binding to serum transferrin (Tf) [10]. Through the portal circulation, ferric iron bound to Tf is transported to sites of use and storage and released by receptor-mediated endocytosis. Uptaken iron is either promptly utilized by the cell or stored into cytosolic

ferritin (Ftn), a protein composed of 24 subunits endowed with ferroxidase activity, able to harbour up to 4,500 iron atoms per molecule as oxy-hydroxide micelles [10].

Iron homeostasis is grossly perturbed during infection and inflammation, leading to iron disorders. In particular, enterocytes and macrophages become iron overloaded, thus increasing the susceptibility of the host to infections, including viral ones [11].

Within this frame, there has been, in the last years, a renewed interest in natural substances, such as lactoferrin (Lf), able to counteract viral infections and at the same time to rebalance iron and inflammatory homeostasis [12, 13]. Lf is an iron-binding glycoprotein belonging to the Tf family. Its structure bears two lobes, lobe N and lobe C, each able to chelate one ferric ion [13]. Most of the *in vitro* and *in vivo* studies have been carried out with bovine Lf (bLf) since it shows about 70% sequence homology and identical functions to human Lf (hLf) [13].

Recently, a multimodal mechanism of action of bLf against SARS-CoV-2 infection has been described, either by its direct binding to host HSPGs [14] and to Spike glycoproteins of SARS-CoV-2 [15] or by modulation of the host cell innate immune response through increased expression of interferon-stimulated genes and TNF-α [16].

Here, to validate the *in silico* results [15], where a direct recognition of the C-terminal domain 1 of the SARS-CoV-2 Spike glycoproteins by both bLf and hLf had been described, we have investigated the Lfs antiviral activity in different epithelial or macrophagic cell models using a Pseudovirus decorated with the Spike protein. In addition, the effect of purified Spike on iron and inflammatory homeostasis in epithelial and macrophagic cell models, in the absence or presence of Lfs, has been analyzed. Moreover, to demonstrate the actual binding between Lfs and Spike, an in vitro pull-down assay was carried out. Finally, *in silico* approaches have been applied to analyze Lfs interactions with TfR1 and the putative binding of bLf to different Spike glycoprotein variants.

Materials and Methods

Bovine and human lactoferrin

Highly purified bLf (Saputo Dairy, Australia) was generously supplied by Vivatis Pharma Italia s.r.l., and highly purified hLf was purchased from Sigma Aldrich (Italy). BLf and hLf purity was about 99% and 97%, respectively, as checked by SDS-PAGE and silver nitrate staining. The concentration of bLf and hLf solutions was assessed via UV spectroscopy with an extinction coefficient of 15.1 (280 nm, 1% solution). Iron saturation was about 11% and 9% for bLf and hLf, respectively, as determined via optical spectroscopy at 468 nm using an extinction coefficient of 0.54 for a 1% solution of 100% iron saturated protein. LPS contamination, assessed via Limulus Amebocyte assay

(Pyrochrome kit, PBI International, Italy), was 0.5 ± 0.06 ng/mg for bLf and 0.3 ± 0.07 ng/mg for hLf. Before each *in vitro* assay, bLf and hLf solutions were sterilized using a 0.2 μm Millex HV filter at low protein retention (Millipore Corp., Bedford, MA, United States).

Cell Culture and virus

The African green monkey kidney–derived Vero E6 and human colon carcinoma–derived Caco-2 cells were purchased from American Type Culture Collection (ATCC), while THP-1 cells, a myelomonocytic cell line derived from the blood of a 1-year-old boy with acute monocytic leukemia, were purchased from European Collection of Cell Cultures (ECACC). Vero E6 and Caco-2 cells were cultured in high-glucose Dulbecco's Modified Eagle's Medium (DMEM) (Euroclone, Italy) with 10% fetal bovine serum (FBS) (Euroclone, Italy) at 37°C in a humidified incubator with 5% CO_2.

THP-1 cells were maintained in RPMI 1640 medium (Euroclone, Italy), supplemented with 10% FBS and 2 mM glutamine, at 37°C in a humidified incubator with 5% CO_2. THP-1 cells, which grow spontaneously in loose suspension under these conditions, were subcultured twice a week by gentle shaking, followed by pelleting and reseeding at a density of approximately $5x10^5$ cells/ml.

SARS-CoV-2 Spike Pseudovirus (hereafter referred to as "Pseudovirus"), an HIV-based luciferase lentivirus pseudotyped with SARS-CoV-2 full length Spike protein of Wuhan strain, was purchased from Creative Biogene (USA). The virus titer is 10^7 transduction units (TU)/ml as determined through HEK293T-ACE2 cell infection.

Infection Assay

For infection assays, cells were seeded in 96-well tissue culture plates (1×10^4 cells/well) for 24 h (Vero E6) or 48 h (Caco-2) at 37°C in a humidified incubator with 5% CO_2. THP-1 cells were differentiated in macrophages by incubation in 96-well tissue culture plates at a density of $2x10^4$ cells/well in RPMI medium containing 0.16 μM phorbol myristate acetate (PMA) (Sigma Aldrich, Italy) for 48 h at 37°C in a humidified incubator with 5% CO_2. To evaluate the inhibition of Pseudovirus infection, 100 and 500 μg/ml of bLf or hLf, corresponding to 1.25 and 6.25 μM, were used on Vero E6 cells, while only the higher concentration was used on Caco-2 and THP-1 cells. For studies on the interaction of bLf or hLf with pseudoviral particles and/or host cells, the infection assay was carried out with a multiplicity of infection (MOI) of 10 in the presence or absence of bLf or hLf, according to the following experimental plan: i) to evaluate the entry efficiency of the pseudoviral particles, cells were infected with Pseudovirus for 8h at 37°C; ii) to evaluate whether bLf or hLf interfere with the viral infectivity rate by binding viral surface components, the Pseudovirus was

preincubated with bLf or hLf for 1 h at 37°C and then the cells were then infected with these suspensions for 8h at 37°C; iii) to evaluate whether bLf or hLf interfere with viral attachment to host cells, cells were preincubated with bLf or hLf for 1 h at 37°C. The cells were then washed with phosphate buffered saline (PBS) and then infected with SARS- CoV-2 Spike Pseudovirus for 8h at 37°C; iv) to assess whether bLf interferes with both viral and host cell components, bLf or hLf was added together with Pseudovirus to cell monolayer for 8h at 37°C.

At the end of the incubation, cells were washed twice with PBS, covered with the appropriate culture medium with 2% of FBS and incubated for 48 h at 37°C in a humidified incubator with 5% CO_2. After 48 h, cells were washed, lysed with cell culture lysis reagent (Promega, Italy) and the transduction efficiency was determined by luminescence analysis using firefly luciferase assay kit (Promega, Italy). The relative luciferase unit (RLU) in each well was detected using Cytation 5 Cell Imaging Multi-Mode Reader (BioTek, Winooski, VT, USA).

Stimulation of Caco-2 and differentiated THP-1 cells with Spike

For the stimulation assay, Caco-2 cells were seeded in 6-well tissue culture plates in complete DMEM medium at a density of 7×10^5 cells/well for 48 h at 37°C in a humidified incubator with 5% CO_2, while THP-1 cells were differentiated in macrophages by incubation in 6-well tissue culture plates at a density of $2x10^6$ cells/well in complete RPMI medium containing 0.16 μM PMA for 48h at 37°C in a humidified incubator with 5% CO_2. Caco-2 cells and differentiated THP-1 cells were washed twice with PBS and treated or not with full-length Spike (Wuhan strain, P2020-025, Trenzyme GmbH, Germany) and/or with bLf according to one of the following experimental procedures: i) untreated cells; ii) cells treated with 100 μg/ml bLf; iii) cells treated with 20 nM Spike; iv) cells pre-treated with 20 nM Spike for 1h and subsequent addition of 100 μg/ml bLf; v) cells pretreated with 100 μg/ml bLf for 1h and subsequent addition of 20 nM Spike and vi) cells treated with a mixture of 100 μg/ml bLf and 20 nM Spike preincubated for 1h. For all conditions, cells were incubated for 48h at 37°C in a humidified incubator with 5% CO_2.

After 48h of incubation, the supernatants were harvested, aliquoted, and stored at −80°C for cytokines quantitation. Adherent cells were scraped in 1 ml of PBS containing 1 mM phenylmethylsulfonyl fluoride (PMSF), pelleted by centrifugation at 5,000 × g for 5 min, and stored at −80°C for protein analysis.

Cytokine analysis

Quantification of IL-1β and IL-6 was performed on cell monolayer supernatants using Human ELISA Max Deluxe Sets (BioLegend, USA).

Western Blots

Caco-2 cells and THP-1 cells were lysed in 300 µl of lysis buffer (25 mM 3-morpholinopropane-1-sulfonic acid pH 7.4/150 mM NaCl/1% Triton containing 1 mM PMSF, 2 µM leupeptin, and pepstatin) in ice for 1 h. Total protein content of samples was measured by Bradford assay. For SDS-PAGE, 20 µg of total protein in SDS sample buffer containing 1,4-dithiothreitol were heat-treated (except for Fpn) and loaded. For Western Blot analysis, primary antibodies used were: monoclonal anti-Fpn 31A5, generously provided by T. Arvedson (Amgen) (1:10000) (Ross et al., 2012), monoclonal anti-TfR1 (anti-TfR) (Santa Cruz, CA, USA) (1:5000), polyclonal anti-Ftn (Santa Cruz, CA, USA) (1:10000), monoclonal anti-actin (Santa Cruz, CA, USA) (1:10000), and polyclonal anti-HCP (Dako, USA) (1:10000) for THP-1, anti-hephaestin (Santa Cruz, CA, USA) (1:10000) for Caco-2, and anti-DMT-1 (Santa Cruz, CA, USA) (1:10000). After incubation with the appropriate secondary Horseradish Peroxidase-conjugated antibody, blots were developed with Enhanced ChemiLuminescence (ECL Prime) (GE Healthcare, UK). Protein levels were normalized on actin by densitometry analysis, performed with ImageJ.

Sepharose 6B pull-down

CNBr-activated Sepharose 6B (GE Healthcare, UK) was employed for conjugation of bLf, hLf or human Transferrin (Fluka). The resin (100 mg) was washed with 1 mM HCl and coupled to 0.5 ml of a 10 mg/ml protein solution in PBS by overnight incubation at room temperature under continuous shaking. The resin was fully inactivated by incubation in 1 ml of Tris-HCl 0.5 M pH 8.0 for 2 h at room temperature. After five washes with 1 ml of PBS, the resins were resuspended in an equal volume of PBS. 40 µl of the resuspended resins were added to 200 µl of full-length Spike of Wuhan strain (20 µg/ml) or its S1 domain (40591-V08H, Sino Biological, Germany) (20 µg/ml) and incubated for 2 h at room temperature under continuous shaking. The resins were then washed five times with 1 ml of PBS and eluted in 50 µl of SDS sample buffer. 20 µl of the eluted fractions were analyzed by SDS-PAGE and Western blot (monoclonal anti-His-HRP, Sigma, 1:10000).

Structures preparations and molecular docking simulations of the TfR1-Lfs complexes

The X-ray structure of TfR1, at a resolution of 1.85 Å, has been extracted from the PDB database (PDB ID: 6OKD) [17]. Three small missing loops in the structure have been modelled using the Modeller software, and the receptor has been minimized in a box of TIP3P water molecules and 0.15 M of NaCl ions, using the ff19SB force field [18] and the AMBER16 software [19]. Representative

structures of bLf and hLf have been extracted from 50 ns MD simulations, performed using the ff19SB force field [18] and the AMBER16 software [19].

Blind protein-protein molecular docking simulations (i.e., no preferential site has been specified) between the TfR1 and the Lfs have been performed using the CLUSPRO web-server (https://cluspro.bu.edu/home.php) [20]. Hydrogen bonds and salt bridges have been analysed using the VMD hbond and salt-bridges modules, while non-polar contacts have been identified using the contact_map routine of the mdtraj Python library [21]. The structure of the Tf-TfR1 complex, used for comparison to the hLf-TfR1 complex, has been extracted from the PDB database (PDBID: 3S9L) [22]. Several Tf regions are missing in the crystallographic structure, including part of its C-lobe region.

Modelling of the SARS-CoV-2 variant structures

The SARS-CoV-2 Spike glycoprotein Alpha, Beta, Delta, and Omicron variant structures have been modelled through Modeller 10.1 using as a reference the original Wuhan strain model used in our previous work [15, 23]. We have taken advantage of the structure modelled in Romeo et al. [23] since the trimer Spike model, composed of three identical monomers, has been already completed by modelling non-terminal missing loops. The mutations, insertions or deletions characterizing the different variants (Table 1) have been introduced based on the data hosted on CoVariants.org, a web resource providing an overview of SARS-CoV-2 variants and mutations that are of interest coming from GISAID data.

Protein-Protein Docking Methods

As described, the Spike Alpha, Beta, Delta, and Omicron variant structures in prefusion conformation were modeled starting from that used in a previously published article [23]. The 3D structure of the diferric form of bLf, refined at 2.8 Å resolution, was downloaded from the PDB database (PDB IDs: 1BLF) [24]. The protein-protein docking analyses between the modeled Spike glycoproteins and the Lf structure were carried out using the Frodock docking algorithm [25]. Frodock's approach combines the projection of the interaction terms into 3D grid-based potentials and the binding energy upon complex formation, which is approximated as a correlation function composed of van der Waals, electrostatics, and desolvation potential terms. The interaction-energy minima are identified through a fast and exhaustive rotational docking search combined with a simple translational scanning [26]. All the docking procedures were performed using Frodock's (http://frodock.chaconlab.org/) webserver.

Molecular Dynamics

Topology and coordinate files of the complexes have been generated through the tLeap module of the AmberTools 21 package [27]. The Spike glycoproteins and Lf have been parametrized through the ff19SB force field [18] and inserted into a triclinic box of TIP3P water molecules, imposing a minimum distance of 12.0 Å from the box walls, while the solution was neutralized adding 0.15 mol/L of NaCl ions. To remove steric interactions, all structures underwent four minimization cycles, each composed of 500 steps of steepest descent minimization followed by 1.500 steps of conjugated gradient minimization. An initial restraint of 20.0 kcal mol^{-1} $Å^{-2}$ was imposed on each protein atom and subsequently reduced and removed in the final minimization cycle. Systems were gradually heated from 0 to 300 K in an NVT ensemble over a period of 5.0 ns using the Langevin thermostat, imposing a starting restraint of 0.5 kcal mol^{-1} $Å^{-2}$ on each atom, which was decreased every 500 ps to relax the system slowly. The systems were simulated in an isobaric-isothermal (NPT) ensemble for 2.0 ns, fixing a pressure of 1.0 atm using the Langevin barostat and imposing the temperature at 300 K. Covalent bonds involving hydrogen atoms were constrained using the SHAKE algorithm [28]. 100 ns of production run were performed through the NAMD 2.13 MD package [29], using a time step of 2.0 fs. The PME method was applied to consider long-range interactions, while a cutoff of 9.0 Å was set for short-range interactions. System coordinates were saved every 1.000 steps.

Trajectory Analysis

Distance analysis has been carried out using the distance module of the GROMACS 2020.4 analysis tools [30], while hydrogen bond and salt bridges persistence has been evaluated using the VMD hbond and salt-bridges modules coupled to in-house written codes. The non-polar contacts were identified using the contact_map and routines of the mdtraj Python library [21]. Generalized Born and surface area continuum solvation (MM/GBSA) analyses were performed over the last 30 ns of the trajectories, through the MMPBSA.py.MPI program as implemented in the AmberTools21 software [19] on two nodes of the ENEA HPC cluster CRESCO6 [31]. Pictures of the Spike-Lf and complexes were generated using the UCSF Chimera program [32].

Statistical analysis

For infection experiments, statistically significant differences were assessed by unpaired student's t test. For Western blots and ELISA assays, the Mann–Whitney U test was used. All statistical analyses were run using Prism v7 software (GraphPad Software, USA). Results were expressed as mean ±

standard deviation (SD) of three independent experiments. A p-value ≤ 0.05 was considered statistically significant.

Results

BLf and hLf have antiviral activity against SARS-CoV-2.

The effect of different concentrations (100 and 500 μg/ml) of bLf and hLf on Pseudovirus infection was initially tested on Vero E6 cells according to the following experimental scheme: i) cells as such infected by Pseudovirus; ii) cells infected by Pseudovirus preincubated with bLf or hLf for 1 h at 37°C; iii) cells preincubated with bLf or hLf for 1h at 37°C before infection by Pseudovirus; iv) cells infected with Pseudovirus added together with bLf or hLf.

BLf exerted a dose-dependent inhibition of pseudoviral infection in all experimental conditions compared to the control, notably when the bLf was preincubated with Pseudovirus or added at the moment of infection (Figure 1A and 1B). HLf also induced at both concentrations tested a significant inhibition of pseudoviral entry in Vero E6 cells compared to the control, particularly when hLf was preincubated with the cells or added at the time of infection. Of note, the inhibition of Pseudovirus entry was invariably lower with hLf than bLf. To prove that the effects of Lfs were not restricted to a specific cell line, we repeated the experiments on epithelial Caco-2 cells and on differentiated macrophagic THP-1 cells with a higher concentration of Lf (500 μg/ml). As shown in Figure 2, comparable results were obtained. In particular, bLf proved to be more efficient than hLf in attenuating Pseudovirus entry into cells.

BLf counteracts inflammatory and iron homeostasis disorders induced by SARS-CoV-2 Spike.

To investigate the role of SARS-CoV-2 Spike on iron and inflammatory disorders and the potential protective effect of bLf, the expression of the main iron-handling proteins and interleukins has been evaluated in both enterocytes and macrophages. For this purpose, Caco-2 and THP-1 cells were treated with 20 nM full length SARS-CoV-2 Spike in the absence or presence of 100 μg/ml bLf, according to the following experimental scheme: i) untreated cells; ii) cells treated with 20 nM Spike glycoprotein; iii) cells treated with 100 μg/ml bLf; iv) cells pre-treated with 20 nM Spike for 1h before addition of 100 μg/ml bLf; v) cells pre-treated with 100 μg/ml bLf for 1h before addition of 20 nM Spike glycoprotein; and vi) cells treated with a mixture of 100 μg/ml bLf and 20 nM Spike preincubated for 1h.

In Caco-2 cells, Spike significantly down-regulated Fpn, Heph and DMT-1 (Figure 3A, B, D), whereas no significant effect on TfR1 and Ftn was recorded (Figure 3C, E). BLf efficiently counteracted this Spike-induced iron dysregulation. For Fpn, Heph and DMT-1 the effect was always evident when a preincubated mixture of bLf and Spike was employed, suggesting that the two proteins likely interact. For Heph and DMT-1, the effect of bLf was significant also on cells preincubated with bLf or treated with bLf 1 h after addition of Spike (Figure 3). This latter result suggests that bLf is

able to reverse the Spike effects even after they have been triggered. On the other hand, TfR1 and Ftn expression did not appear to be affected by Spike (Figure 3C, E). Of note, no detectable levels of IL-1β and IL-6 were recorded both in basal and Spike/bLf-stimulated conditions (data not shown).
As observed with Caco-2, Spike induced a significant down-regulation of the iron exporter Fpn in macrophagic THP-1 cells and, again, bLf easily counteracted the effect in all conditions tested (Figure 4A). We also measured the molecular partner of Fpn, namely the membrane-bound ferroxidase ceruloplasmin (Cp), which was found to be positively affected by Spike treatment. bLf was able also in this case, to bring Cp levels back to those of untreated cells (Figure 4B). No Ftn modulation was detected upon Spike challenge (Figure 4D), while, at variance with Caco-2, a significant up-regulation (reversed by bLf) of TfR1 was observed in this case (Figure 4C). As shown in Figure 4E and F, Spike induced a significant up-regulation of both IL-1β and IL-6, the main cytokines involved in iron disorders. BLf counteracted the increase, its effect being significant when the bLf was preincubated with Spike and, for IL-6, even when added to cells before Spike (Figure 4F).

BLf and hLf bind to SARS-CoV-2 Spike.

To test whether bLf and hLf directly bind to SARS-CoV-2 Spike, an *in vitro* pull-down assay has been carried out. We prepared bLf-, hLf- and hTf-conjugated Sepharose 6B and the resins were then incubated with either full-length Spike or its S1 domain (unconjugated Sepharose was used as control). As shown in Figure 5A, when SDS-eluted fractions of both bLf- and hLf-conjugated resins were probed with an anti-His Antibody (tag for Spike glycoprotein), an immuno-reactive band with molecular mass around 250 kDa was present, consistently corresponding to the trimeric form of the viral glycoprotein. Of note, no reactive bands were recorded for both unconjugated and hTf-conjugated resins, thus demonstrating the specificity of the binding between Spike and bLf/hLf. The S1 domain of Spike did not appear to be sufficient to bind Lfs, as demonstrated by the absence of immunoreactive bands in the corresponding SDS-eluted fraction (Figure 5B).

Molecular docking simulations of Tfr-1 in complex with bovine and human lactoferrin

As already stated, Lf has been extensively demonstrated to block viral entry by competing with virus structure and/or cell surface receptors. Moreover, SARS-CoV-2 has been reported to exploit multiple cell surface receptors for its entry, including TfR1 [33]. Due to the high identity between Lf and Tf, the natural TfR1 interactor, we evaluated the possibility that the blocking of Spike-mediated viral entry could also be linked to Lf competition with TfR1. On this basis, we performed molecular docking simulations between TfR1 and Lfs.

Main molecular docking binding pose obtained for the TFR1-hLf complex is reported in Figure 6A. In this binding pose, hLf localizes at the helical and protease-like domains of TfR1, at the interface of the two monomers, almost completely overlapping the Tf binding site on TfR1, as determined by X-ray crystallography (PDB ID: 3S9L) [22] (Figure 6B, 7). HLf interacts with 48 TfR1 residues, establishing 6 hydrogen bonds and 11 salt bridges (Table 2). In particular, 17 of these residues are also contacted by Tf in the crystallographic Tf-TfR1 complex (Table 2), confirming that both proteins contact equivalent regions on the TfR1 surface (Figure 7).

Main molecular docking binding pose obtained for the TfR1-bLf complex is reported in Figure 8. In this complex, bLf contacts the apical domain of TfR1 with its N-terminal lobe. A crystallographic structure retrieved from the PDB (PDB ID: 3KAS) [34] revealed that this TfR1 region is also the binding site of the trimeric GP1 surface glycoproteins of the MACV, JUNV, GTOV and SABV arenaviruses, responsible for haemorrhagic fevers in humans. The binding of GP1 surface glycoproteins to TFR1 allows virus internalization into endosomes [34]. The interactions established by bLf at this site, including 12 non-polar contacts and 7 salt bridges, are reported in Table 2.

Computational results on bLf and Spike variants

The molecular docking simulations between bLf and the four Spike variants of interest (Alpha, Beta, Delta, and Omicron) indicate a preferential binding pose in which the bLf structure interacts with the RBD domain in the up conformation (Figure 9). For all the four docking simulations, the first three solutions obtained by docking clustering procedure account for more than 60-70% of the total generated complexes, which are superimposable to the binding pose obtained in our previous work [15]. Using as a starting structure the first solutions obtained from docking experiments, we performed four 100 ns long classical MD simulations in order to verify the stability of the complexes, to check for the presence of persistent interactions and to verify the ability of bLf to interact with all the Spike variants regardless of the number and position of the mutations.

As shown in Figure 10, the distance between the centers of mass of the four Spike glycoproteins and bLf, calculated as a function of time, oscillates around the value of 4.5 nm, indicating a constantly close contact between the two molecules for all the simulation time. MM/GBSA analyses confirmed the high affinity of the bLf for the Spike glycoprotein (Table 3), showing an interaction energy of -36.2, -69.1, -46.4 and -45.8 kcal/mol for the Alpha, Beta, Delta, and Omicron Spike variants, respectively. Interestingly, MM/GBSA results underlined that the energy term mainly contributing to the binding energy switches from the Van der Waals term for the Alpha variant (as observed for the Wuhan isolate) [15] to the polar solvation term for the Omicron. This suggests that, although the

recognition occurs with similar orientations of the interacting partners, the detected interactions defining the complexes significantly differ for the four studied variants.

A detailed analysis of the interaction networks, reported in Table 4, revealed an increase in high-persistence hydrogen bonds and salt bridges between Spike and bLf, going from the Alpha variant to Omicron. For the Alpha variant, we observed 94 different interactions, which persist for more than 40% of the simulation time, consisting of 3 salt bridges, 4 hydrogen bonds and 87 residue pairs involved in non-polar contacts (Table 4 and 5, Alpha column). For the Beta variant, the number of high-persistence interactions increases to 113, with 4 salt bridges, 4 hydrogen bonds and 105 residue pairs involved in non-polar contacts (Table 4 and 5, Beta column). As expected from the MM/GBSA results, we observed an increase in polar and charged interactions for the Delta and Omicron variants, with 5 salt bridges and 6 and 7 hydrogen bonds, respectively (Table 4, Delta and Omicron columns). On the other hand, there is a reduction of non-polar contacts, with 100 and 70 residue pairs involved in these interactions (Table 5, Delta and Omicron columns). Remarkably, in the case of Omicron, four out of five reported salt bridges involve variant-specific mutations.

These results allow us to hypothesize that bLf should retain its ability to bind the surface of the Spike glycoprotein, independently of the mutations observed for the variants of concern emerged so far.

Discussion

The severity of CoV infections is mainly regulated by and dependent on the Spike glycoprotein, which, along with cell tropism and infectivity, regulates viral spread and host responses. Although the receptor binding domains of Spike from SARS-CoV-2 and SARS-CoV share ca. 75% amino acid identity, the two viruses show significant differences in their ability to infect and transmit in humans [35]. Interestingly, recent papers have questioned the possible role of Spike in contributing to the higher virulence of SARS-CoV-2 [35]. Indeed, Spike is emerging as the main virulence factor of SARS-CoV-2, able to induce host immunopathogenesis, which is, in turn, the critical regulator of virus infection and disease outcomes [35]. For this reason, all efforts in the last 2 years have focused on discovering substances capable of interacting with Spike and, in turn, inhibiting SARS-CoV-2 infection.

In this respect, the *in silico* results reported in the paper by Campione and colleagues [15] had indicated Lf as an ideal candidate for counteracting SARS-CoV-2 infection due to its putative ability to bind to the C-terminal domain of Spike. To validate such a model, we have therefore studied the antiviral activity of human and bovine Lf against a Pseudovirus decorated with the SARS-CoV-2 Spike protein, in two epithelial and a macrophagic cell lines. The results clearly show that

Pseudovirus entry into cells is invariably inhibited by Lfs, with minor variations in terms of concentration dependence, Lf source, experimental protocol, and cell line. It is interesting to note that bLf exerts a more potent inhibition compared to hLf. This strengthens the use of the bovine form as a therapeutic agent. The highest decrease in Pseudoviral entry was observed when bLf and Pseudovirus were added together, with or without pre-incubation. This is a good indication that bLf may physically interact with Spike and that this is the molecular mechanism at the basis of the inhibitory effect exerted by Lfs against SARS-CoV-2. In other terms, bLf hinders Spike-mediated virus entry by competitive inhibition of Spike-mediated virus binding to host receptors, with an efficacy likely depending on cell-specific expression of different plasma membrane receptors in different cell lines which modulate SARS-CoV-2 entry rate.

As already reported, SARS-CoV-2 Spike alone has been shown to induce a potent pro-inflammatory response via TLR2-dependent activation of the NF-kB pathway in *in vitro* models [5]. In this context, the role of iron, a transition metal involved in many fundamental biological processes, including DNA/RNA synthesis and ATP generation, must be taken into account. As a matter of fact, higher iron availability, strictly associated with inflammatory disorders, has been shown to promote viral spread, which requires active cell metabolism, as demonstrated for the human immunodeficiency virus (HIV) [36], where it is involved in several key steps of virus replication, from the reverse transcription process to the iron-dependent production of dNTPs [37]. Moreover, iron is implicated in the activation of NF-kB signaling by generation of reactive oxygen species (ROS) [38]. Recently, it has been also reported that SARS-CoV-2 replication is dependent on host cell iron-related enzymes, some of which are involved in transcription, viral mRNA translation, and viral assembly [39].

Here, for the first time, we demonstrate that SARS-CoV-2 Spike glycoprotein can induce dysregulation of some of the main iron-handling proteins, both in enterocytes and macrophages. In particular, a significant down-regulation of Fpn was found in both models tested, thus suggesting a possible induction of intracellular iron retention. This hypothesis was further corroborated by the down-regulation of DMT-1 and Heph in the enterocytes and by the up-regulation of TfR1 in the macrophagic model. Overall, the observed changes agree with previous studies on iron proteins and inflammation, particularly with the acute phase response [6]. Indeed, the decrease in Fpn expression upon inflammatory challenge has been widely reported in several *in vitro* models [40, 41] and confirmed in animal studies [42, 43]. Such an effect is usually linked to the induction of pro-inflammatory cytokines, in particular IL-1β and IL-6, in partnership or not with the hepcidin pathway [44]. Notably, Spike treatment has induced an opposite effect on Fpn functional partners, Cp and Heph. Along with the down-regulation of Heph in enterocytes, the up-regulation of Cp in macrophages was observed. To understand this difference, we should recall that, besides the shared

function of iron oxidase, Cp has been described as endowed with multiple functions, ranging from copper transport to biological amines oxidation, to antioxidant activity exerted through several different mechanisms [10]. Moreover, Cp and Heph are differently regulated at the translational level [45]. Cp is an inflammatory, acute-phase plasma protein produced by hepatocytes and monocyte/macrophages, induced by inflammation or iron loading [46]. The cell type-specific regulation of Cp expression has been demonstrated in myeloid lineage, showing Cp synthesis to be successfully induced by TNF-α in alveolar macrophages [47] and in monocytic cell lines by IFN-γ [48]. Moreover, Persichini and colleagues [49] reported the up-regulation of Cp, both in the secreted and GPI-linked forms, upon treatment with IL-1β in a glial cellular model [49]. Our results lie in this framework, with the Spike protein able to induce Cp expression in concordance with its ability to up-regulate pro-inflammatory response in THP-1 cells. On the other side, Heph (and DMT-1) down-regulation in Caco-2 cells is consistent with a pro-inflammatory challenge, as already reported in some studies [50, 51]. Regarding TfR1, its significant up-regulation in THP-1 cells following Spike treatment is in line with other studies reporting increased expression during acute phase response [52, 53]. Moreover, despite its role in iron uptake, TfR1 is also hijacked by numerous viruses to enter the cell [11], and SARS-CoV-2 does not seem to be an exception [33]. Therefore, TfR1 up-regulation can both act as a SARS-CoV-2 gate for its cell entry and favour viral metabolism and replication through iron intake. Intriguingly, concerning the potential iron-retention phenotype, both enterocyte and macrophage models did not significantly increase intracellular Ftn. Hepatocytes, macrophages and Kupffer cells have been shown to secrete Ftn [54], which is enhanced by iron and pro-inflammatory cytokines [55]. Interestingly, Tran and colleagues [55] demonstrated, in a murine model of acute phase response, that the administration of IL-1β or TNF-α doubled the amounts of secreted Ftn, while it did not influence intracellular Ftn levels [55]. New recent evidence on COVID-19 patients shows that serum Ftn levels are increased as the disease worsens, providing a potential indication of the mortality risk [56, 57]. However, despite the robust association with mortality, whether hyper-ferritinemia is a mere systemic marker of disease progression or a key modulator in disease pathogenesis is yet to be clarified.

In this scenario, we demonstrated that bLf protects host cells from iron and inflammatory disorders in different conditions. Beyond the blockade of Spike-induced pathogenesis through direct binding, here demonstrated for the first time *in vitro*, and competition with cell surface receptors when pre-incubated with both cell monolayer or the viral glycoprotein, bLf can rebalance iron and inflammatory disorders even when acting after the Spike challenge.

In recent years, our group has demonstrated the efficacy of bLf in reverting iron dysregulation in different inflamed/infected in vitro [41, 58] and in vivo [59] models as well as in clinical trials [44].

Such an effect on iron homeostasis can be related to Lf's ability to chelate free iron and downregulate pro-inflammatory cytokines, such as IL-1β and IL-6, thus boosting anti-oxidant and anti-inflammatory host response to viral infection.

Other than Spike involvement in the dysregulation of iron proteins in both enterocytes and macrophages and the bLf protective effect on such disorders, here, we show evidence at a mechanistic level that both hLf and bLf can interact with the trimeric form of a full-length SARS-CoV-2 Spike glycoprotein. To date, the Lf efficacy in inhibiting SARS-CoV-2 entry was mostly associated with its ability to interact with the host cell surface molecules, of which heparan sulfates were demonstrated to be the most involved [14]. Through this study, we expanded our *in silico* model, recently published [15], and validated it through in vitro pull-down assay, allowing us to affirm that Lfs can consistently block SARS-Co-V-2 entry also through its direct binding to Spike glycoprotein. Further, to atomistically understand the molecular mechanisms through which Lfs can block viral entry, we performed molecular docking simulations with TfR1. Results suggest that the TfR1 surface represents a promising binding site for both the human and bovine Lfs. Remarkably, the binding pose obtained for the human form strikingly resembles that adopted by Tf, the natural binder of TfR1, both in orientation and interaction pattern. BLf doesn't achieve the same binding pose but contacts a completely different region, the apical domain of TfR1, known to be the binding site of different "New World" arenaviruses. The binding of these viruses to the TfR1 apical domain allows their internalization into the host cell. However, despite these promising docking results and the high sequence and structural similarity between Tf and Lfs, it should be noted that experimental evidence suggests very low levels of binding between bLf and TfR1 [60].

Finally, the results obtained from molecular docking between bLf and Spike variants strongly suggest that the ability of bLf to interact with Spike is not influenced by single point mutations, that occur in the more widespread genetic variants. This finding further promotes the potential use of bLf in the early stages of SARS-CoV-2 infection.

In conclusion, our data corroborate the results of our preliminary clinical trials [61, 62] where, with the caveat of the limited number of Lf-treated patients, it was observed that a prompt bLf treatment decreases i) the time to SARS-CoV-2 RNA negativization (14-15 versus 24-28 days) [61, 62]; ii) the clinical symptoms recovery [62]; iii) serum IL-6, Ftn and D-dimers levels [62]. In addition, a very interesting link between symptom reduction and age was observed: the protective effect of Lf in reducing the time to symptom resolution is related to advancing age [61].

Further studies need to be carried out to ascertain the *in vivo* efficacy of Lfs in SARS-CoV-2 infection and sequelae. Yet, our results give hope for its employment as a prompt adjuvant of the standard therapies.

References

1. Lu R, Zhao X, Li J, Niu P, Yang B, Wu H, Wang W, Song H, Huang B, Zhu N, et al (2020) Genomic Characterisation and Epidemiology of 2019 Novel Coronavirus: Implications for Virus Origins and Receptor Binding. The Lancet 395(10224):565-574. doi: 10.1016/S0140-6736(20)30251-8
2. Walls AC, Park YJ, Tortorici MA, Wall A, McGuire AT, Veesler D (2020) Structure, Function, and Antigenicity of the SARS-CoV-2 Spike Glycoprotein. Cell 181(2):281-292.e6. doi: 10.1016/j.cell.2020.02.058
3. Hoffmann M, Kleine-Weber H, Schroeder S, Kruger N, Herrler T, Erichsen S, Schiergens TS, Herrler G, Wu NH, Nitsche A, et al (2020) SARS- CoV-2 Cell Entry Depends on ACE2 and TMPRSS2 and Is Blocked by a Clinically Proven Protease Inhibitor. Cell 181(2):271-280.e8. doi: 10.1016/j.cell.2020.02.052.
4. Liu F, Li L, Xu M, Wu J, Luo D, Zhu Y, Li B, Song X, Zhou X (2020) Prognostic value of interleukin-6, C-reactive protein, and procalcitonin in patients with COVID-19. J Clin Virol 127:104370. doi: 10.1016/j.jcv.2020.104370
5. Patra T, Meyer K, Geerling L, Isbell TS, Hoft DF, Brien J, Pinto AK, Ray RB, Ray R (2020) SARS-CoV-2 Spike protein promotes IL-6 trans-signaling by activation of angiotensin II receptor signaling in epithelial cells. PLoS Pathog 16(12):e1009128. doi: 10.1371/journal.ppat.1009128
6. Ganz T, Nemeth E (2015) Iron homeostasis in host defence and inflammation. Nat Rev Immunol 15(8):500-510. doi: 10.1038/nri3863.
7. Frazer DM, Anderson GJ (2003) The orchestration of body iron intake: how and where do enterocytes receive their cues? Blood Cells Mol Dis 30:288–297. doi:10.1016/S1079-9796(03)00039-1
8. Mackenzie B, Garrick MD (2005) Iron imports: II. Iron uptake at the apical membrane in the intestine. Am J Physiol Gastrointest Liver Physiol 289:G981–986. doi:10.1152/ajpgi.00363.2005
9. Donovan A, Lima CA, Pinkus JL, Pinkus GS, Zon LI, Robine S, Andrews NC (2005) The iron exporter ferroportin/Slc40a1 is essential for iron homeostasis. Cell Metab 1:191–200. doi:10.1016/j.cmet.2005.01.003
10. Bonaccorsi di Patti MC, Cutone A, Polticelli F, Rosa L, Lepanto MS, Valenti P, Musci G (2018) The ferroportin-ceruloplasmin system and the mammalian iron homeostasis machine: Regulatory pathways and the role of lactoferrin. Biometals 31(3):399-414. doi: 10.1007/s10534-018-0087-5
11. Mancinelli R, Rosa L, Cutone A, Lepanto MS, Franchitto A, Onori P, Gaudio E, Valenti P (2020) Viral Hepatitis and Iron Dysregulation: Molecular Pathways and the Role of Lactoferrin. Molecules 25(8):1997. doi: 10.3390/molecules25081997.
12. Valenti P, Antonini G (2005) Lactoferrin: an important host defence against microbial and viral attack. Cell Mol Life Sci 62(22):2576-2587. doi: 10.1007/s00018-005-5372-0
13. Rosa L, Cutone A, Lepanto MS, Paesano R, Valenti P (2017) Lactoferrin: A Natural Glycoprotein Involved in Iron and Inflammatory Homeostasis. Int J Mol Sci 18(9):1985. doi: 10.3390/ijms18091985
14. Hu Y, Meng X, Zhang F, Xiang Y, Wang J (2021) The in vitro antiviral activity of lactoferrin against common human coronaviruses and SARS-CoV-2 is mediated by targeting the heparan sulfate co-receptor. Emerg Microbes Infect 10(1):317-330. doi: 10.1080/22221751.2021.1888660
15. Campione E, Lanna C, Cosio T, Rosa L, Conte MP, Iacovelli F, Romeo A, Falconi M, Del Vecchio C, Franchin E, et al (2021) Lactoferrin against SARS-CoV-2: In vitro and in silico evidences. Front Pharmacol 12:666600. doi: 10.3389/fphar.2021.666600
16. Mirabelli C, Wotring JW, Zhang CJ, McCarty SM, Fursmidt R, Pretto CD, Qiao Y, Zhang Y, Frum T, Kadambi NS, et al (2021) Morphological cell profiling of SARS-CoV-2 infection

identifies drug repurposing candidates for COVID-19. Proc Natl Acad Sci U S A 118(36):e2105815118. doi: 10.1073/pnas.2105815118
17. Crook ZR, Girard E, Sevilla GP, Merrill M, Friend D, Rupert PB, Pakiam F, Nguyen E, Yin C, Ruff RO, et al (2020) A TfR-Binding Cystine-Dense Peptide Promotes Blood–Brain Barrier Penetration of Bioactive Molecules. J Mol Biol 432(14):3989-4009. doi: 10.1016/j.jmb.2020.04.002.
18. Tian X, Li C, Huang A, Xia S, Lu S, Shi Z, Lu L, Jiang S, Yang Z, Wu Y, et al. (2020) Potent Binding of 2019 Novel Coronavirus Spike Protein by a SARS Coronavirus-specific Human Monoclonal Antibody. Emerg Microbes Infect 9(1):382-385. doi: 10.1080/22221751.2020.1729069
19. Case D, Betz R, Cerutti D, Cheatham T, Darden T, Duke R, et al (2016) Amber 2016. San Fr: Univ. California.
20. Kozakov D, Hall DR, Xia B, Porter KA, Padhorny D, Yueh C, Beglov D, Vajda S (2017) The ClusPro web server for protein-protein docking. Nat Protoc 12(2):255-278. doi: 10.1038/nprot.2016.169.
21. McGibbon RT, Beauchamp KA, Harrigan MP, Klein C, Swails JM, Hernández CX, Schwantes CR, Wang LP, Lane TJ, Pande VS (2015) MDTraj: A Modern Open Library for the Analysis of Molecular Dynamics Trajectories. Biophys J 109(8):1528-32. doi: 10.1016/j.bpj.2015.08.015
22. Eckenroth BE, Steere AN, Chasteen ND, Everse SJ, Mason AB (2011) How the binding of human transferrin primes the transferrin receptor potentiating iron release at endosomal pH. Proc Natl Acad Sci U S A 108(32):13089-13094. doi: 10.1073/pnas.1105786108
23. Romeo A, Iacovelli F, Falconi M (2020) Targeting the SARS-CoV-2 Spike Glycoprotein Prefusion Conformation: Virtual Screening and Molecular Dynamics Simulations Applied to the Identification of Potential Fusion Inhibitors. Virus Res 286:198068. doi: 10.1016/j.virusres.2020.198068
24. Moore SA, Anderson BF, Groom CR, Haridas M, Baker EN (1997). Three-dimensional Structure of Diferric Bovine Lactoferrin at 2.8 Å Resolution. J Mol Biol 274(2):222-236. doi: 10.1006/jmbi.1997.1386
25. Ramírez-Aportela E, López-Blanco JR, Chacón P (2016) FRODOCK 2.0: Fast Protein-Protein Docking Server. Bioinformatics 32:2386–2388. doi:10.1093/bioinformatics/btw141
26. Garzon JI, Lopéz-Blanco JR, Pons C, Kovacs J, Abagyan R, Fernandez-Recio J, Chacon P (2009) FRODOCK: a New Approach for Fast Rotational Protein-Protein Docking. Bioinformatics 25(19):2544-51. doi:10.1093/bioinformatics/btp447
27. Salomon-Ferrer R, Case DA, Walker RC (2013) An Overview of the Amber Biomolecular Simulation Package. WIREs Comput Mol Sci 3:198–210. doi:10.1002/wcms.1121
28. Ryckaert JP, Ciccotti G, Berendsen HJC (1977) Numerical Integration of the Cartesian Equations of Motion of a System with Constraints: Molecular Dynamics of N-Alkanes. J Comput Phys 23:327–341. doi:10.1016/0021- 9991(77)90098-5
29. Phillips JC, Braun R, Wang W, Gumbart J, Tajkhorshid E, Villa E, Chipot C, Skeel RD, Kalé L, Schulten K (2005) Scalable Molecular Dynamics with NAMD. J Comput Chem 26(16):1781-802. doi: 10.1002/jcc.20289
30. Abraham MJ, Murtola T, Schulz R, Páll S, Smith JC, Hess B, Lindahl E (2015) GROMACS: High Performance Molecular Simulations through Multi-Level Parallelism from Laptops to Supercomputers. SoftwareX 1- 2(2):19–25. doi:10.1016/j.softx.2015.06.001
31. Iannone F, Ambrosino F, Bracco G, De Rosa M, Funel A, Guarnieri G, Migliori S, Palombi F, Ponti G, Santomauro G, et al. (2019. "CRESCO ENEA HPC Clusters: a Working Example of a Multifabric GPFS Spectrum Scale Layout," in 2019 International Conference on High Performance Computing & Simulation (HPCS), Dublin, Ireland, 1051–1052. doi:10.1109/HPCS48598.2019.9188135

32. Pettersen EF, Goddard TD, Huang CC, Couch GS, Greenblatt DM, Meng EC, Ferrin TE (2004) UCSF Chimera--A Visualization System for Exploratory Research and Analysis. J Comput Chem 25(13):1605-1612. doi:10.1002/jcc.20084
33. Tang X, Yang M, Duan Z, Liao Z, Liu L, Cheng R, Fang M, Wang G, Liu H, Xu J, Kamau PM, Zhang Z, Yang L, Zhao X, Peng X, Lai R (2020) Transferrin receptor is another receptor for SARS-CoV-2 entry. bioRxiv. doi: https://doi.org/10.1101/2020.10.23.350348
34. Abraham J, Corbett KD, Farzan M, Choe H, Harrison SC (2010) Structural basis for receptor recognition by New World hemorrhagic fever arenaviruses. Nat Struct Mol Biol 17(4):438-444. doi: 10.1038/nsmb.1772.
35. Saadi F, Pal D, Sarma JD (2021) Spike Glycoprotein Is Central to Coronavirus Pathogenesis-Parallel Between m-CoV and SARS-CoV-2. Ann Neurosci 28(3-4):201-218. doi: 10.1177/09727531211023755
36. Schmidt SM (2020) The role of iron in viral infections. Front Biosci (Landmark Ed) 25:893-911. doi: 10.2741/4839
37. Romeo AM, Christen L, Niles EG, Kosman DJ (2001) Intracellular chelation of iron by bipyridyl inhibits DNA virus replication: ribonucleotide reductase maturation as a probe of intracellular iron pools. J Biol Chem 276(26):24301-24308. doi: 10.1074/jbc.M010806200
38. Xiong S, She H, Takeuchi H, Han B, Engelhardt JF, Barton CH, Zandi E, Giulivi C, Tsukamoto H (2003) Signaling role of intracellular iron in NF-kappaB activation. J Biol Chem 278(20):17646-54. doi: 10.1074/jbc.M210905200
39. Sienkiewicz M, Jaśkiewicz A, Tarasiuk A, Fichna J (2021) Lactoferrin: an overview of its main functions, immunomodulatory and antimicrobial role, and clinical significance. Crit Rev Food Sci Nutr 8:1-18. doi: 10.1080/10408398.2021.1895063.
40. Recalcati S, Locati M, Marini A, Santambrogio P, Zaninotto F, De Pizzol M, Zammataro L, Girelli D, Cairo G (2010) Differential regulation of iron homeostasis during human macrophage polarized activation. Eur J Immunol 40(3):824-35. doi: 10.1002/eji.200939889.
41. Cutone A, Rosa L, Lepanto MS, Scotti MJ, Berlutti F, Bonaccorsi di Patti MC, Musci G, Valenti P (2017) Lactoferrin Efficiently Counteracts the Inflammation-Induced Changes of the Iron Homeostasis System in Macrophages. Front Immunol 8:705. doi: 10.3389/fimmu.2017.00705.
42. Liu XB, Nguyen NB, Marquess KD, Yang F, Haile DJ (2005) Regulation of hepcidin and ferroportin expression by lipopolysaccharide in splenic macrophages. Blood Cells Mol Dis 35(1):47-56. doi: 10.1016/j.bcmd.2005.04.006
43. Willemetz A, Beatty S, Richer E, Rubio A, Auriac A, Milkereit RJ, Thibaudeau O, Vaulont S, Malo D, Canonne-Hergaux F (2017) Iron- and Hepcidin-Independent Downregulation of the Iron Exporter Ferroportin in Macrophages during Salmonella Infection. Front Immunol 8:498. doi: 10.3389/fimmu.2017.00498
44. Lepanto MS, Rosa L, Cutone A, Conte MP, Paesano R, Valenti P (2018) Efficacy of Lactoferrin Oral Administration in the Treatment of Anemia and Anemia of Inflammation in Pregnant and Non-pregnant Women: An Interventional Study. Front Immunol 9:2123. doi: 10.3389/fimmu.2018.02123
45. Mazumder B, Sampath P, Fox PL (2006) Translational control of ceruloplasmin gene expression: beyond the IRE. Biol Res 39(1):59-66. doi: 10.4067/s0716-97602006000100007
46. Marques L, Auriac A, Willemetz A, Banha J, Silva B, Canonne-Hergaux F, Costa L (2012) Immune cells and hepatocytes express glycosylphosphatidylinositol-anchored ceruloplasmin at their cell surface. Blood Cells Mol Dis 48(2):110-120. doi: 10.1016/j.bcmd.2011.11.005
47. Tisato V, Gallo S, Melloni E, Celeghini C, Passaro A, Zauli G, Secchiero P, Bergamini C, Trentini A, Bonaccorsi G, et al (2018) TRAIL and Ceruloplasmin Inverse Correlation as a Representative Crosstalk between Inflammation and Oxidative Stress. Mediators Inflamm 2018:9629537. doi: 10.1155/2018/9629537

48. Mazumder B, Mukhopadhyay CK, Prok A, Cathcart MK, Fox PL (1997) Induction of ceruloplasmin synthesis by IFN-gamma in human monocytic cells. J Immunol 159(4):1938-44.
49. Persichini T, Maio N, di Patti MC, Rizzo G, Toscano S, Colasanti M, Musci G (2010) Interleukin-1β induces ceruloplasmin and ferroportin-1 gene expression via MAP kinases and C/EBPβ, AP-1, and NF-κB activation. Neurosci Lett 484(2):133-138. doi: 10.1016/j.neulet.2010.08.034.
50. Sheikh N, Dudas J, Ramadori G (2007) Changes of gene expression of iron regulatory proteins during turpentine oil-induced acute-phase response in the rat. Lab Invest 87(7):713-725. doi: 10.1038/labinvest.3700553
51. Bergamaschi G, Di Sabatino A, Pasini A, Ubezio C, Costanzo F, Grataroli D, Masotti M, Alvisi C, Corazza GR (2017) Intestinal expression of genes implicated in iron absorption and their regulation by hepcidin. Clin Nutr 36(5):1427-1433. doi: 10.1016/j.clnu.2016.09.021
52. Malik IA, Naz N, Sheikh N, Khan S, Moriconi F, Blaschke M, Ramadori G (2011) Comparison of changes in gene expression of transferrin receptor-1 and other iron-regulatory proteins in rat liver and brain during acute-phase response. Cell Tissue Res 344(2):299-312. doi: 10.1007/s00441-011-1152-3.
53. Tacchini L, Gammella E, De Ponti C, Recalcati S, Cairo G (2008) Role of HIF-1 and NF-kappaB transcription factors in the modulation of transferrin receptor by inflammatory and anti-inflammatory signals. J Biol Chem 283(30):20674-20686. doi: 10.1074/jbc.M800365200
54. Wesselius LJ, Nelson ME, Skikne BS (1994) Increased release of ferritin and iron by iron-loaded alveolar macrophages in cigarette smokers. Am J Respir Crit Care Med 150(3):690-695. doi: 10.1164/ajrccm.150.3.8087339
55. Tran TN, Eubanks SK, Schaffer KJ, Zhou CY, Linder MC (1997) Secretion of ferritin by rat hepatoma cells and its regulation by inflammatory cytokines and iron. Blood 90(12):4979-4986. https://doi.org/10.1182/blood.V90.12.4979
56. Mehta P, McAuley DF, Brown M, Sanchez E, Tattersall RS, Manson JJ (2020) COVID-19: Consider cytokine storm syndromes and immunosuppression. Lancet 395(10229):1033-1034. doi: 10.1016/S0140-6736(20)30628-0
57. Phua J, Weng L, Ling L, Egi M, Lim CM, Divatia JV, Shrestha BR, Arabi YM, Ng J, Gomersall CD, et al (2020) Intensive care management of coronavirus disease 2019 (COVID-19): challenges and recommendations. Lancet Respir Med 8(5):506–517. doi: 10.1016/S2213-2600(20)30161-2
58. Frioni A, Conte MP, Cutone A, Longhi C, Musci G, di Patti MC, Natalizi T, Marazzato M, Lepanto MS, Puddu P, et al (2014) Lactoferrin differently modulates the inflammatory response in epithelial models mimicking human inflammatory and infectious diseases. Biometals 27(5):843-856. doi: 10.1007/s10534-014-9740-9
59. Cutone A, Lepanto MS, Rosa L, Scotti MJ, Rossi A, Ranucci S, De Fino I, Bragonzi A, Valenti P, Musci G, et al. (2019) Aerosolized Bovine Lactoferrin Counteracts Infection, Inflammation and Iron Dysbalance in A Cystic Fibrosis Mouse Model of *Pseudomonas aeruginosa* Chronic Lung Infection. Int J Mol Sci 20(9):2128. doi: 10.3390/ijms20092128.
60. Kawabata H, Tong X, Kawanami T, Wano Y, Hirose Y, Sugai S, Koeffler HP (2004) Analyses for binding of the transferrin family of proteins to the transferrin receptor 2. Br J Haematol 127(4):464-473. doi: 10.1111/j.1365-2141.2004.05224.x
61. Rosa L, Tripepi G, Naldi E, Aimati M, Santangeli S, Venditto F, Caldarelli M, Valenti P (2021) Ambulatory COVID-19 Patients Treated with Lactoferrin as a Supplementary Antiviral Agent: A Preliminary Study. J Clin Med 10(18):4276. doi: 10.3390/jcm10184276.
62. Campione E, Lanna C, Cosio T, Rosa L, Conte MP, Iacovelli F, Romeo A, Falconi M, Del Vecchio C, Franchin E, et al (2021) Lactoferrin as Antiviral Treatment in COVID-19 Management: Preliminary Evidence. Int J Environ Res Public Health 18(20):10985. doi: 10.3390/ijerph182010985.

Statements and Declarations

Funding

This study was supported by the contribution of "Fondazione Terzo Pilastro Internazionale", President Prof. Emmanuele Francesco Maria Emanuele to Elena Campione and by University of Rome La Sapienza Funds to Maria Pia Conte.

Competing Interests

No competing interests do declare.

Author Contributions

All authors contributed to the study conception and design. Material preparation, data collection and analysis were performed by all authors. The first draft of the manuscript was written by Antimo Cutone, Luigi Rosa and Mattia Falconi and all authors commented on previous versions of the manuscript. All authors read and approved the final manuscript.

Data Availability

The datasets generated during and/or analysed during the current study are available from the corresponding author on reasonable request.

Ethics approval

Not applicable.

Consent to participate

Not applicable.

Consent to publish

Not applicable.

Variant of concern	Defining mutations
B.1.1.7 (Alpha)	ΔH69-V70, ΔY144, N501Y, A570D, D614G, P681H, T716I, S982A, D1118H
B.1.351 (Beta)	D80A, D215G, ΔL241-L242-A243, K417N, E484K, N501Y, D614G, A701V
B.1.617.2 (Delta)	T19R, ΔE156-F157, R158G, L452R, T478K, D614G, P681R, D950N
B.1.1.529 (Omicron)	A67V, ΔH69-V70, T95I, ΔG142-V143-Y144, Y145D, ΔN211, L212I, G339D, S371L, S373P, S375F, K417N, N440K, G446S, S477N, T478K, E484A, Q493R, G496S, Q498R, N501Y, Y505H, T547K, D614G, H655Y, N679K, P681H, N764K, D796Y, N856K, Q954H, N969K, L981F

Table 1. The mutations, insertions or deletions characterizing the different variants simulated in this work.

TfR1-hLf	TfR1-bLf
Hydrogen bonds	**Hydrogen bonds**
K385.B - Q512	/
R646.A - C371	/
S654.A - E388	/
R121.A - Q165	/
G661.A - Y65	/
Y123.A - Q165	/
Salt bridges	**Salt bridges**
D755.A - K73	D245.B - K27
K508.A - E335	D352.B - R21
K508.A - E336	D356.B - K28
E623.A -E366	K205.B - E176
R183.B - E514	R208.B – E178
K385.B - E514	E369.B - R186
E606.A - R332	E369.B - R38
E612.A - K333	/
R629.A - E637	/
K633.A - E637	/
E664.A - R120	/
Non-polar contacts	**Non-polar contacts**
S120.A: P167	D245: K28
Y123.A: P144, E146, A147, F166	Y247: R20, Q23, W24, K27
W124.A: T139, E143	T248: R20, W24
D125.A: E143, R151	E350: Q13, W16, F17, R20
K508.A: T139, S334	G351: F17, W24
Q511.A: E336	D352: R25, S285
K600.A: P142	C353: R25
N608.A: P142	P354: R25, K28
L619.A: N359, S362, G363, G367, T370	S355: R25
R623.A: Q360, G363, L364	M365: W24
D626.A: Q360	V366: R20, W24
R629.A: S636	E369: W16
Q640.A: E352, E353, R356	/
Y643.A: L355, R356, N359	/
R646.A: L355, N359	/
G647.A: L355	/
F650.A: V346, T370, C371, S372	/
R651.A: S373	/
T658.A: E388	/
F660.A: R332	/
G661.A: I328	/
D662.A: Y65, L69	/
A663.A: L69	/
E664.A: L69	/
K665.A: R332	/
V670.A: A70	/
E163.B: Q512, G513, E514	/
K177.B: N52, N261	/
Q185.B: E514	/
F187.B: Q512	/
K394.B: P71, Y72	/

Table 2. Hydrogen bonds, salt bridges and non-polar interactions established between TfR1 (monomer A and B) and hLf or bLf. TfR1 residues highlighted in grey are also contacted by Tf in the Tf-TfR1 crystallographic structure (PDB ID: 3S9L).

MM/GBSA results					
Variant	**VdW (kcal/mol)**	**Electrostatic (kcal/mol)**	**Nonpolar solvation (kcal/mol)**	**Polar solvation (kcal/mol)**	**$\Delta G_{binding}$ (kcal/mol)**
B.1.1.7	-181.5 ± 11.1	-22.9 ± 47.6	-22.6 ± 1.8	190.7 ± 49.5	-36.2 ± 8.8
B.1.351	-175.3 ± 12.4	280.1 ± 56.0	-22.5 ± 1.8	-151.4 ± 54.8	-69.1 ± 13.5
B.1.617.2	-164.9 ± 9.2	473.13 ± 56.5	-22.1 ± 1.2	-332.4 ± 53.1	-46.4 ± 8.3
B.1.1.529	-156.7 ± 10.1	836.9 ± 51.6	-21.6 ± 1.1	-758.8 ± 47.7	-45.8 ± 11.0

Table 3. Results of the MM/GBSA analyses performed over the last 30 ns of the Spike-bovine lactoferrin complex simulation for the four variants of concern.

B.1.1.7 (Alpha)	B.1.351 (Beta)	B.1.617.2 (Delta)	B.1.1.529 (Omicron)
Salt bridges			
D443 - K458A	K358 - D398A	K358 - D405A	D646 - K440B
D126 - K444A	E352 - K444C	K642 - D467A	E355 - R498C
E574 - K444B	E407 - K444C	E355 - R409A	E356 - R498C
	D646 - K444B	D646 - K444B	E654 - R498B
		E355 - K378A	K358 - D405A
Hydrogen bonds			
N349 - Y501A	E356- N449C	Q386 - N439C	K358 - D405A
Q628 - E406A	S160 - F490C	N387 - T500C	E356 - R498C
H439 - Y439A	S381 - N440C	D646 - K444B	E355 - R498C
Q386 - N465C	Q378 - N440C	Q386 - Q506C	E356 - S496C
		C390 - N440C	D646 - K440B
		E355 - R408A	R363 - F497C
			Q386 - Q506C

Table 4. Salt bridges and hydrogen bond interactions established between the bovine lactoferrin and the surface of the Spike glycoprotein (chain A, B or C), calculated for the four variants of concern. Only interactions identified for more than 40% of simulation time are shown. Residues highlighted in grey corresponds to variant-specific mutations.

B.1.1.7 (Alpha)	B.1.351 (Beta)	B.1.617.2 (Delta)	B.1.1.529 (Omicron)
Non-polar contacts			
K627: D402A, R405A, Q411A, T412A, G413A	C377: W436C, N437C, S438C, N439C, N440C	G641: F462A, R464A	T576: F494B
L630: Q411A	S381: W436C, S438C, Y505C	K642: N437B	C644: N436B
L631: P409A, G410A, Q411A, P497C	W380: S438C, N439C	C644: S441B, P497B	P645: N436B
H632: P497C	G385: S438C, G496C, F497C, Q498C, P499C, T500C, Y505C	P645: S436B, N437B, D440B, S441B, F495B, Q496B, P497B, T498B	S653: F494B, R495B, P496B
Q634: Q411A	K376: N439C	D646: S436B, N437B, P497B, T498B, Y503B	L151: G499A
A635: P497C, T498C	N387: N439C	K647: P497B	R152: R495A, P496A, T497A, Y498A, G499A
L636: T498C	V388: N439C, K444C, G496C	F648: P497B	P153: R495A, P496A, T497A
K642: T498C	T389: N439C, K444C	F651: F495B, Q496B, P497B	L155: R495A
P645: G499B	E373: N440C	S653: F495B, Q496B	S156: G499A
D646: T498C, G500C	E355: S443C, K444C, G446C, G447C, Y495C, G496C	L125: Q496A	W157: H502A
S653: P496B	T362: S443C, K444C, V445C, G446C, G447C, G496C, F497C, Q498C	L151: G500A	E159: C477C
A668: D417A	A359: K444C, V445C, G446C	R152: N499A, G500A, G502A, Y503A	S160: P476C, C477C, N484C
Q124: Q495A	V364: K444C, V445C	P153: Q496A, G502A, Y503A	T353: G499A, V500A
L125: S440A	C390: K444C	L155: W434A	A354: G401A, F494C
M148: P496A, T497A	G406: K444C, V445C	W157: C486C	E355: Y492C, F494C
G149: Q495A, P496A, T497A, G501A	L347: V445C	E159: C486C, L490C	V357: I399A, G401A, G499A, V500A, G501A
R152: G501A, Y502A	R351: V445C, G446C, G447C, N448C	S160: S369A, N485C, C486C	K358: F494C, R495C
P153: S435A, Q495A, G501A	E352: N448C	L251: P497A	Y361: R495C
C250: F494A, Q495A, P496A	A184: G476C	N252: Q496A, P497A	T362: S493C, F494C, R495C
L251: F494A, Q495A	S160: P479C, C480C, F486C, N487C, C488C, Y489C, S371A	L347: V443C	Q374: N436C
N252: Q495A	E159: C488C, Y489C, L492C	R351: G444C, N446C	C377: S435C, N436C, D439C
S341: T497A	K358: G496C, Q498C	E352: N446C	Q378: G499B
L344: T497A	S384: F497C, Q498C, P499C, T500C	T353: G500A	W380: S493C
T345: T497A	Y361: Q498C	A354: V405A	S381: Y498C
K348: T497A, Y498A	Q386: Q498C, P499C	E355: V405A, N446C, G494C	S384: F494C, R495C, P496C, T497C, Y498C
E356: G499A	Q383: P499C	V357: G402A, V405A	G385: S493C, F494C, R495C, P496C, T497C, H502C
V357: G499A	W157: S371A	K358: V405A, Q496C	Q386: R495C, P496C
K358: K442C, G494C	A354: F374A, V407A	Y361: P497C	N387: S493C
R360: T497A, Y498A, G499A	V357: V407A	T362: G445C, G494C, Q496C	V388: S493C

Y361: V404A, G494C, Q496C	P645: W437B, S439B, N440B, Y506B	E373: N437C	T389: D439C, S440C, K441C
T362: K442C, G494C	C644: S439B, N440B, S444B, Q499B	K376: N437C	C390: K441C
C377: N437C	D646: S439B, T501B, Y506B	C377: N435C, S436C, N437C, N438C	A391: K441C
S381: S436C, N437C, D440C, Y499C, Y503C	S575: F498B	Q378: P497B, T498B, N499B	V401: K441C
Q382: P497C, T498C, Y499C	S653: F498B, T501B	W380: S436C, N437C	G406: K441C
Q383: Q496C, P497C, T498C, Y499C	F648: Q499B, P500B	S381: G500B, W434C, S436C, Y503C	S575: V442B, F494B
S384: G494C, F495C, Q496C, P497C, T498C, Y499C	F651: Q499B, P500B	Q382: G500B, Y503B	
G385: S436C, D440C, K442C, G494C, Q496C	K375: P500B	S384: Q496C, P497C, T498C, N499C	
Q386: Q496C, P497C	Q378: P500B, T501B, Y502B, G503B	G385: W434C, S436C, G494C, F495C, Q496C, P497C, T498C, Y503C	
S437: E468A, I469A	K647: P500B	Q386: Q496C, P497C, T498C	
K438: E468A, I469A	K652: P500B	V388: N437C, G494C	
	Q382: G503B, Y506B	T389: N437C	
		C390: K442C	
		V401: K442C	
		G406: K442C, V443C	

Table 5. Non-polar interactions established between the bovine lactoferrin and the Spike glycoprotein surface (chain A, B or C), calculated for the four variants of concern. Only interactions identified for more than 40% of simulation time are shown.

Legends to Figures

Fig 1 Luminescence of Pseudovirus observed in Vero E6 cells infected at multiplicity of infection (MOI) of 10 in the presence or absence of 100 μg/ml (a,c) or 500 μg/ml (b,d) of bovine lactoferrin (bLf) (a,b) or human lactoferrin (hLf) (c,d). See text for details. Data represent the mean values of three independent experiments. Error bars: standard error of the mean. Statistical significance is indicated as follows: **: $p<0.001$, ***: $p<0.0001$ (unpaired student's t test). RLU = relative luminescence unit

Fig 2 Luminescence of Pseudovirus observed in Caco-2 (a,b) and THP-1 (c,d) cells infected at multiplicity of infection (MOI) of 10 in the presence or absence of 500 μg/ml of bovine lactoferrin (bLf) (a,c) or human lactoferrin (hLf) (b,d). See text for details. Data represent the mean values of three independent experiments. Error bars: standard error of the mean. Statistical significance is indicated as follows: **: $p<0.001$, ***: $p<0.0001$ (unpaired student's t test). RLU = relative luminescence unit

Fig 3. Protective effect of bovine lactoferrin (bLf) against iron and inflammatory disorders induced by SARS-CoV-2 Spike glycoprotein on Caco-2 cells. Western blot and densitometry analysis of ferroportin (Fpn) (a), hephaestin (b), transferrin receptor 1 (TfR1) (c), DMT-1 (d) and ferritin (Ftn) (e) levels in Caco-2 cells untreated or treated with 20 nM Spike glycoprotein in the absence or presence of 100 μg/ml bovine lactoferrin (bLf). See text for details. Error bars: standard error of the mean. Statistical significance is indicated as follows: *: $p < 0.05$; **: $p < 0.01$ (unpaired t-test)

Fig 4 Protective effect of bovine lactoferrin (bLf) against iron and inflammatory disorders induced by SARS-CoV-2 Spike glycoprotein on THP-1 cells. Western blot and densitometry analysis of ferroportin (Fpn) (a), membrane-bound ceruloplasmin (Cp) (b), transferrin receptor 1 (TfR1) (c) and ferritin (Ftn) (d) levels and ELISA quantitation of IL-1β (e) and IL-6 (f) production in THP-1 cells untreated or treated with 20 nM Spike glycoprotein in the absence or presence of 100 μg/ml bovine lactoferrin (bLf). See text for details. Error bars: standard error of the mean. Statistical significance is indicated as follows: *: $p < 0.05$; **: $p < 0.01$ (unpaired t-test)

Fig 5 Sepharose 6B pull down of full-length (a) and RBD (b) SARS-CoV-2 Spike. Unconjugated (-), bLf-, hLf- and hTf-conjugated Sepharose 6B resins were employed. Input, unbound (U) and SDS eluted fractions were analyzed through Western blot

Fig 6 a) Complex between hLf (in red) and TfR1 (in grey) obtained through molecular docking simulations. **b)** Superposition of the hLf-TfR1 docking pose with the Tf-TfR1 crystallographic structure (PDB ID: 3S9L)

Fig 7 Comparison between the Tf-TfR1 crystallographic structure (PDB ID: 3S9L) and the obtained hLf-TfR1 docking pose. Both TfR1 monomers are represented in grey; Tf is represented with a blue transparent surface bound to TfR1 monomer A, while hLf in red bound on TfR1 monomer B. Both TfR1 monomers are equivalent for sequence, structure and interactions, Tf and hLf can therefore occupy the same location

Fig 8 Complex obtained between bLf (in blue) and TfR1 (in grey). The apical domain of TfR1, binding site of bLf, is highlighted in red. A closer representation of the interaction site is shown in the right image, where the proteins are represented as a solid surface, except for the interacting regions that are shown as cartoons

Fig 9 Complex between bLf and the four Spike variants of interest obtained through molecular docking simulations. bLf is represented with yellow ribbons, while the three different chains composing the Spike glycoprotein are represented by red, blue, and green ribbons

Fig 10 Time-dependent analysis of the distance evaluated between the centres of mass of the bLf and the RBD domain in the up conformation of the four Spike variants (black: Alpha, red: Beta, green: Delta and blue: Omicron)

Figures

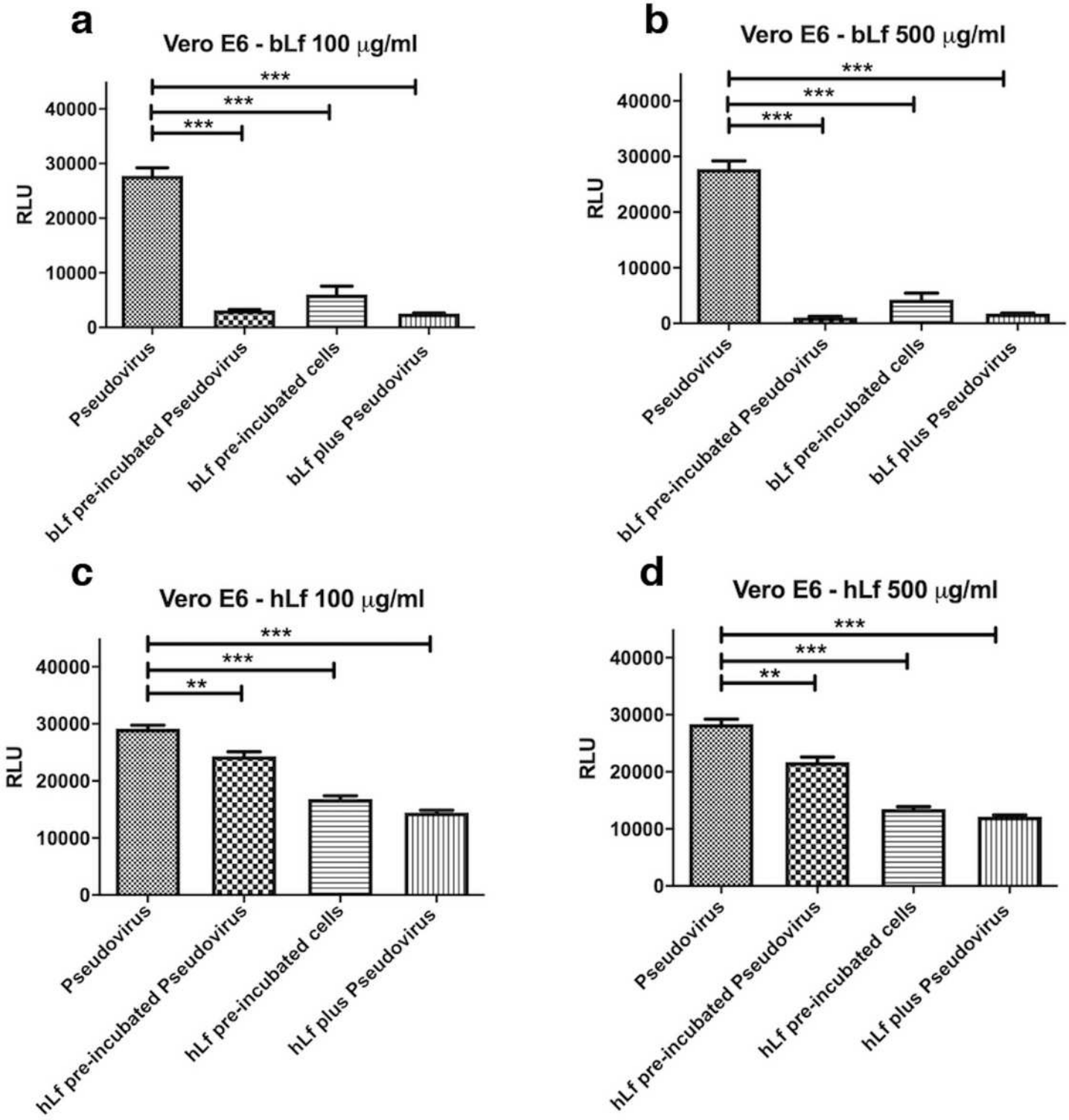

Figure 1

Luminescence of Pseudovirus observed in Vero E6 cells infected at multiplicity of infection (MOI) of 10 in the presence or absence of 100 µg/ml (a,c) or 500 µg/ml (b,d) of bovine lactoferrin (bLf) (a,b) or human lactoferrin (hLf) (c,d). See text for details. Data represent the mean values of three independent

experiments. Error bars: standard error of the mean. Statistical significance is indicated as follows: **: p<0.001, ***: p<0.0001 (unpaired student's t test). RLU = relative luminescence unit

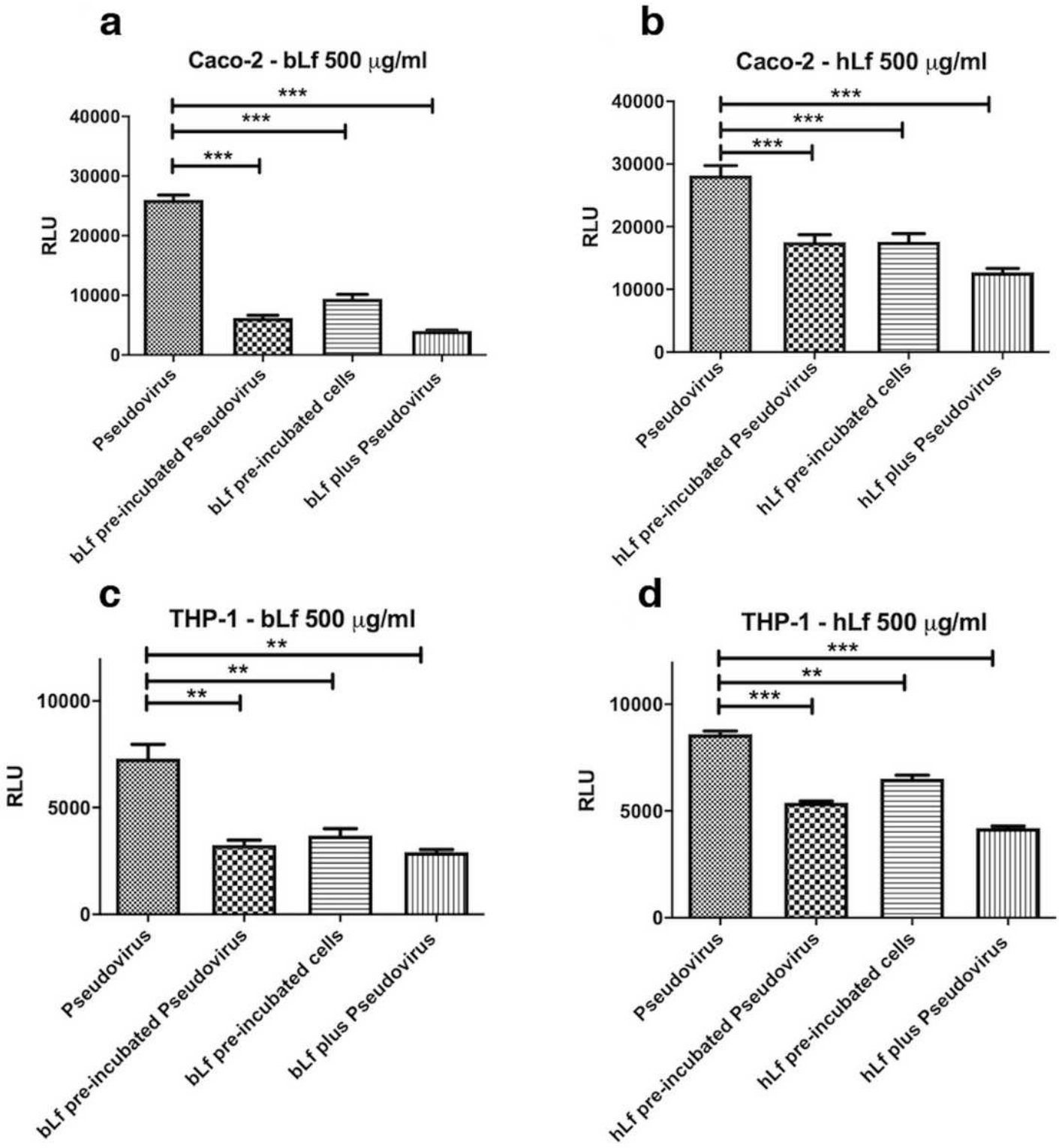

Figure 2

Luminescence of Pseudovirus observed in Caco-2 (a,b) and THP-1 (c,d) cells infected at multiplicity of infection (MOI) of 10 in the presence or absence of 500 μg/ml of bovine lactoferrin (bLf) (a,c) or human

lactoferrin (hLf) (b,d). See text for details. Data represent the mean values of three independent experiments. Error bars: standard error of the mean. Statistical significance is indicated as follows: **: p<0.001, ***: p<0.0001 (unpaired student's t test). RLU = relative luminescence unit

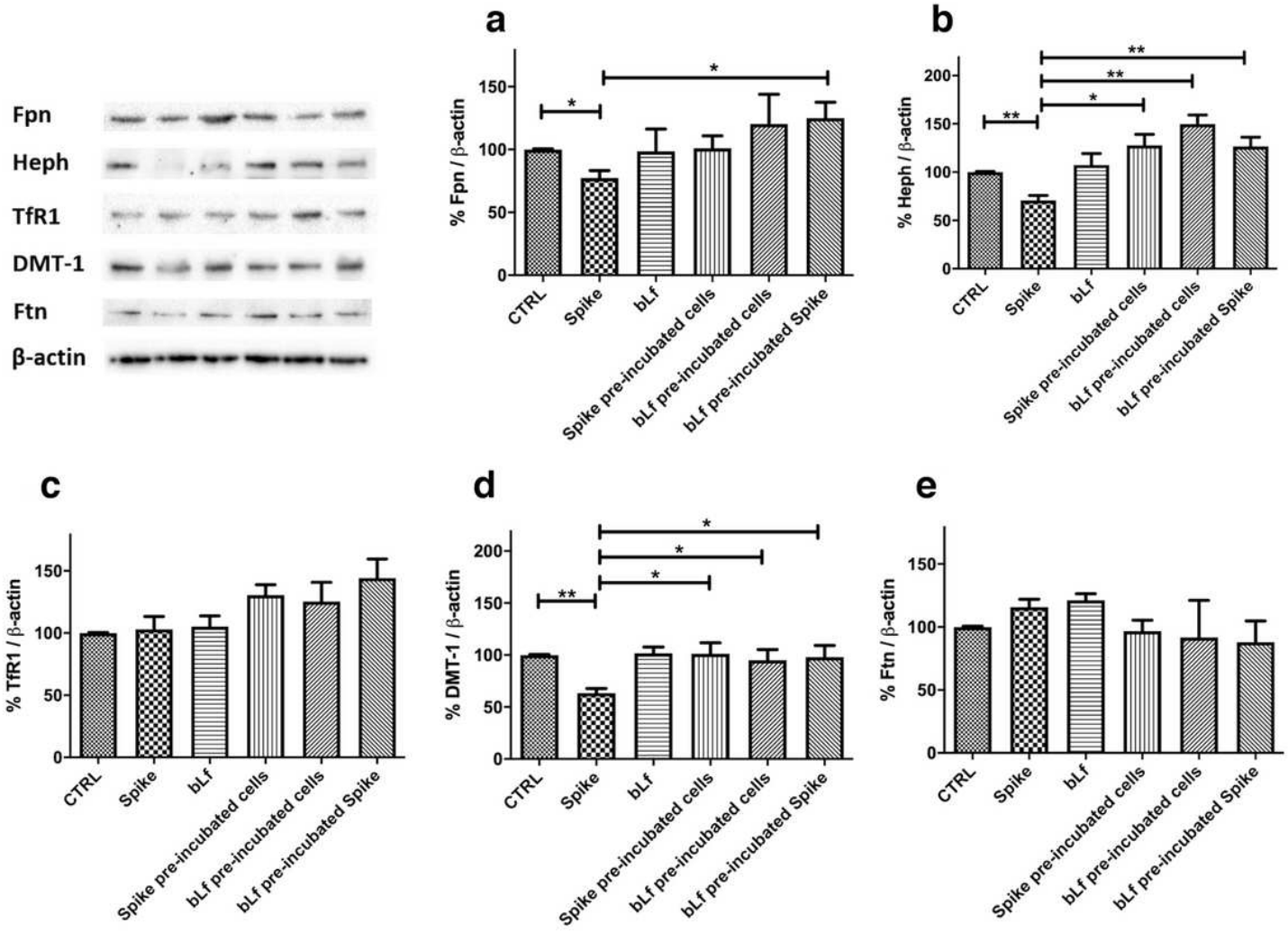

Figure 3

Protective effect of bovine lactoferrin (bLf) against iron and inflammatory disorders induced by SARS-CoV-2 Spike glycoprotein on Caco-2 cells. Western blot and densitometry analysis of ferroportin (Fpn) (a), hephaestin (b), transferrin receptor 1 (TfR1) (c), DMT-1 (d) and ferritin (Ftn) (e) levels in Caco-2 cells untreated or treated with 20 nM Spike glycoprotein in the absence or presence of 100 µg/ml bovine lactoferrin (bLf). See text for details. Error bars: standard error of the mean. Statistical significance is indicated as follows: *: $p < 0.05$; **: $p < 0.01$ (unpaired t-test)

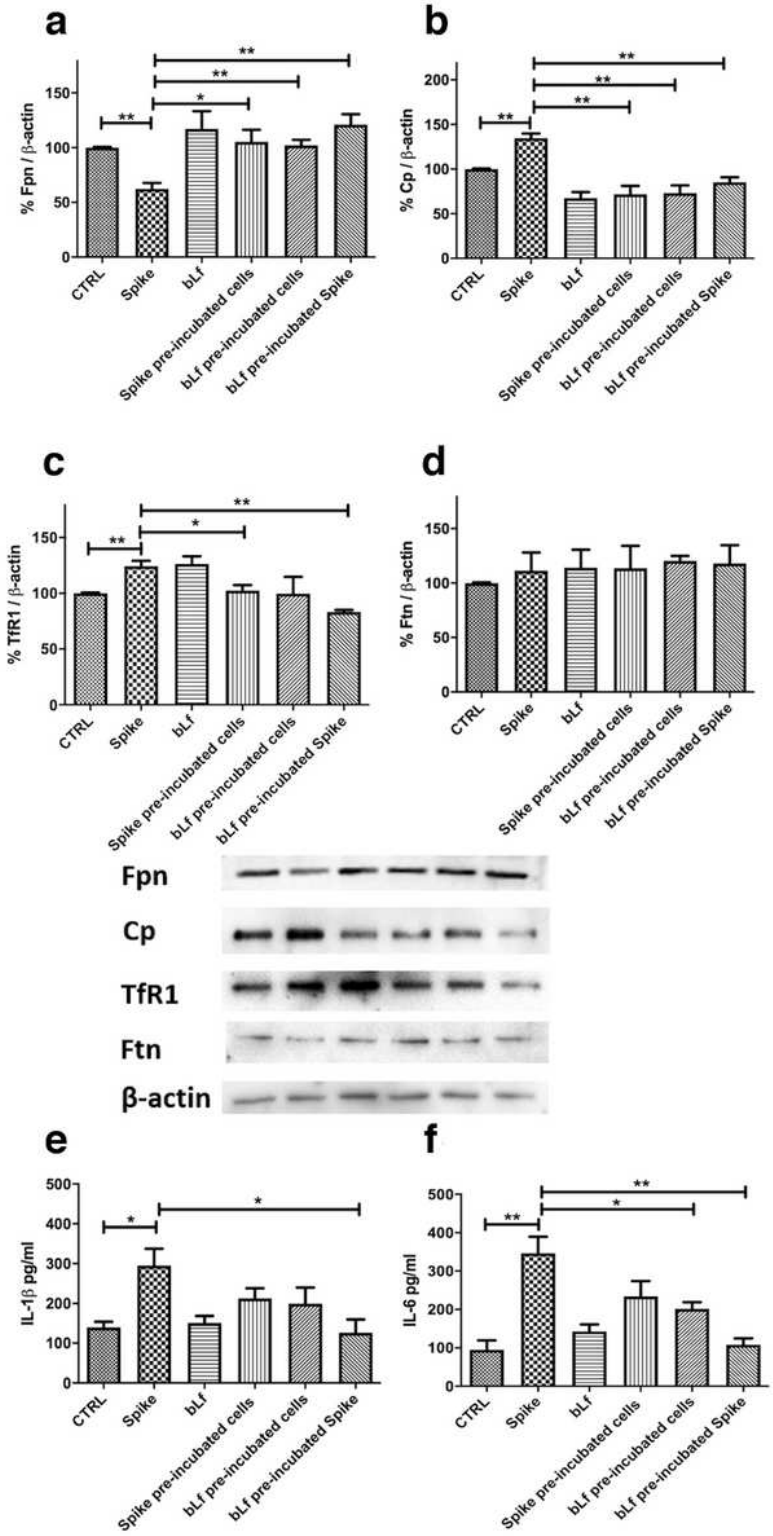

Figure 4

Protective effect of bovine lactoferrin (bLf) against iron and inflammatory disorders induced by SARS-CoV-2 Spike glycoprotein on THP-1 cells. Western blot and densitometry analysis of ferroportin (Fpn) (a), membrane-bound ceruloplasmin (Cp) (b), transferrin receptor 1 (TfR1) (c) and ferritin (Ftn) (d) levels and ELISA quantitation of IL-1β (e) and IL-6 (f) production in THP-1 cells untreated or treated with 20 nM Spike glycoprotein in the absence or presence of 100 μg/ml bovine lactoferrin (bLf). See text for details.

Error bars: standard error of the mean. Statistical significance is indicated as follows: *: $p < 0.05$; **: $p < 0.01$ (unpaired t-test)

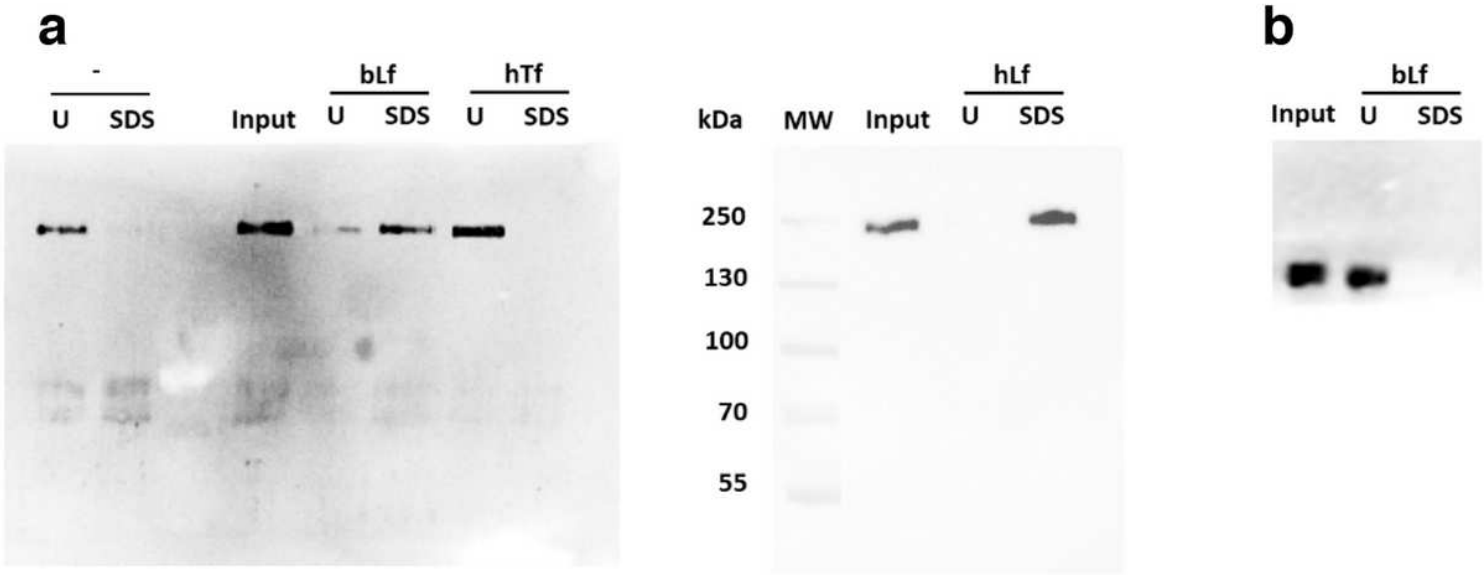

Figure 5

Sepharose 6B pull down of full-length (a) and RBD (b) SARS-CoV-2 Spike. Unconjugated (-), bLf-, hLf- and hTf-conjugated Sepharose 6B resins were employed. Input, unbound (U) and SDS eluted fractions were analyzed through Western blot

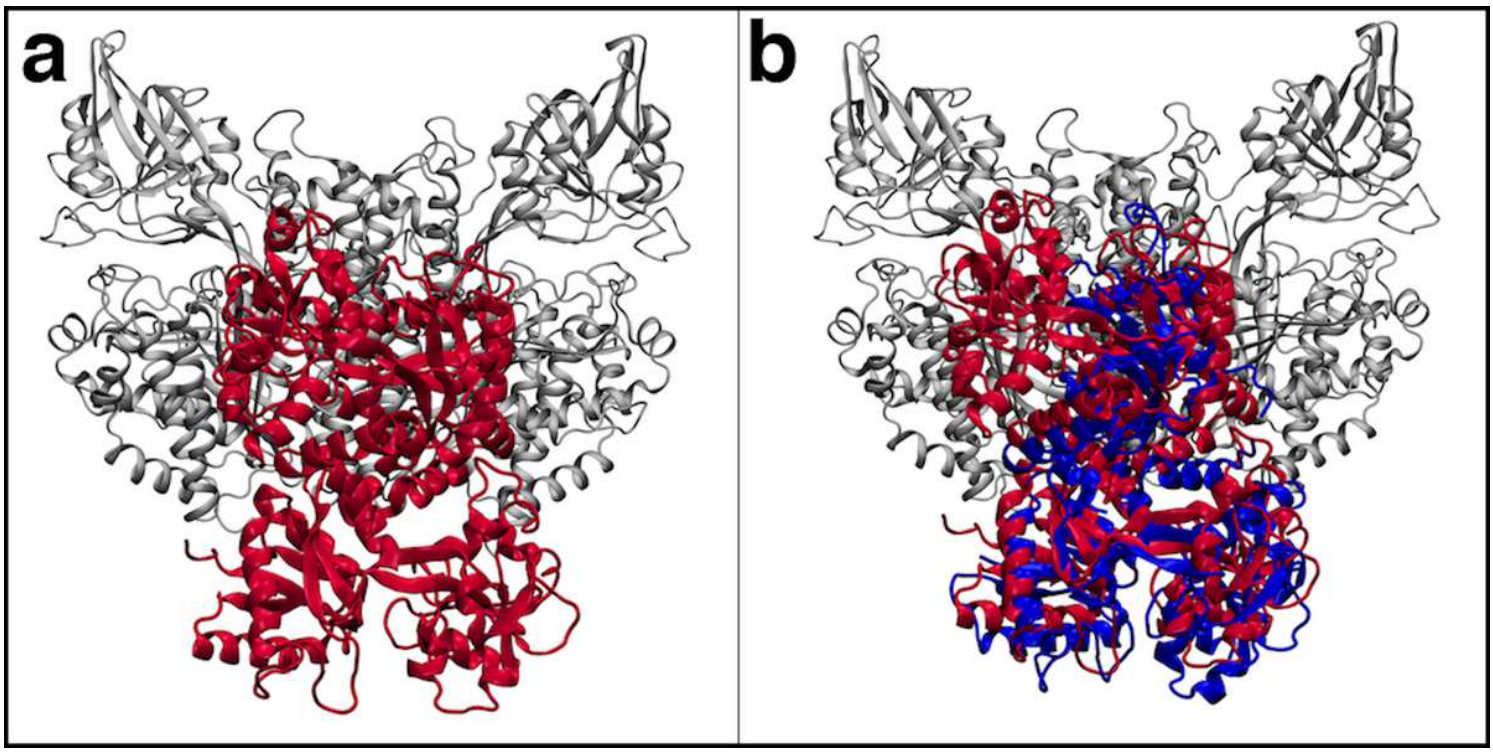

Figure 6

a) Complex between hLf (in red) and TfR1 (in grey) obtained through molecular docking simulations. b) Superposition of the hLf-TfR1 docking pose with the Tf-TfR1 crystallographic structure (PDB ID: 3S9L)

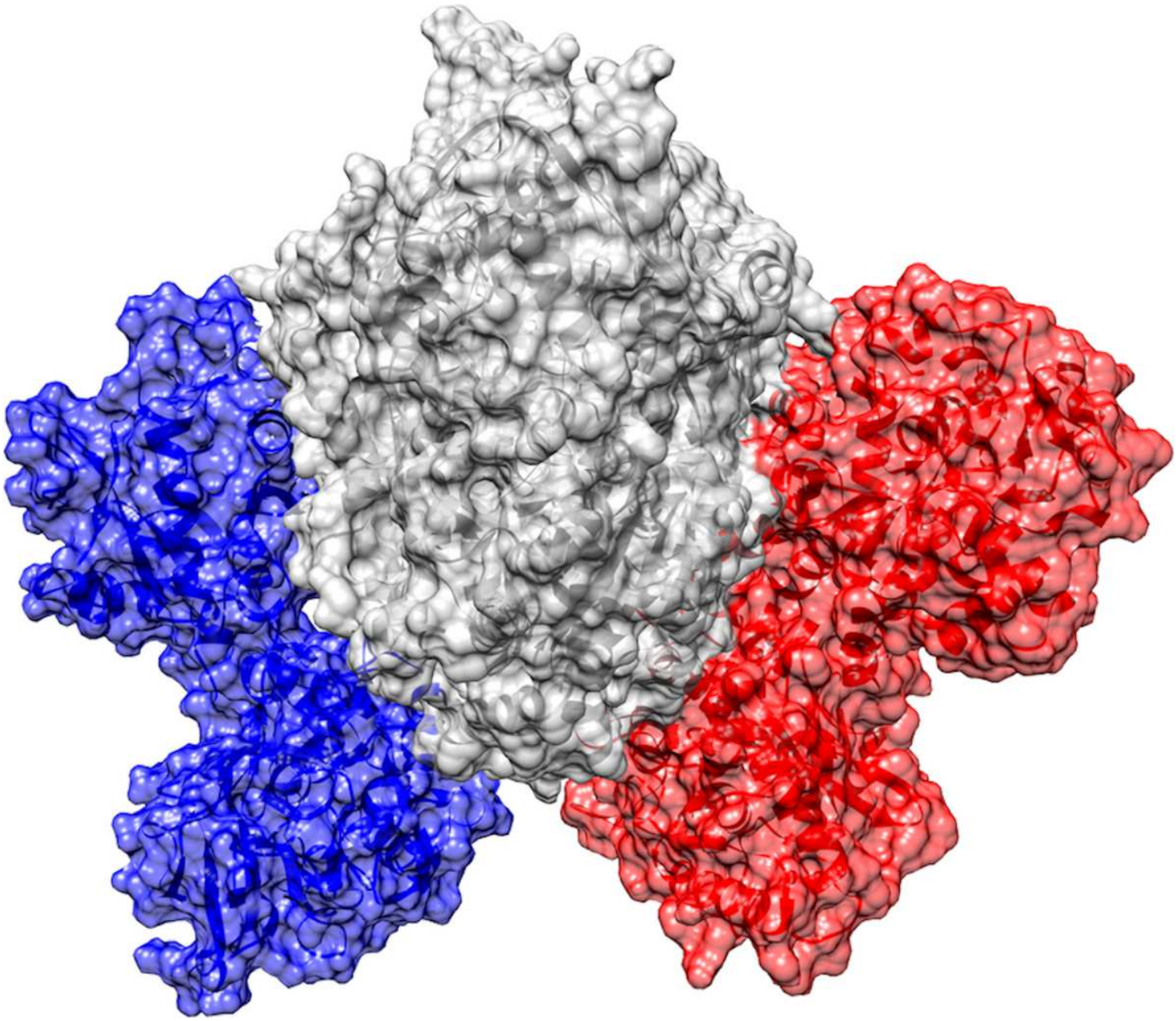

Figure 7

Comparison between the Tf-TfR1 crystallographic structure (PDB ID: 3S9L) and the obtained hLf-TfR1 docking pose. Both TfR1 monomers are represented in grey; Tf is represented with a blue transparent surface bound to TfR1 monomer A, while hLf in red bound on TfR1 monomer B. Both TfR1 monomers are equivalent for sequence, structure and interactions, Tf and hLf can therefore occupy the same location

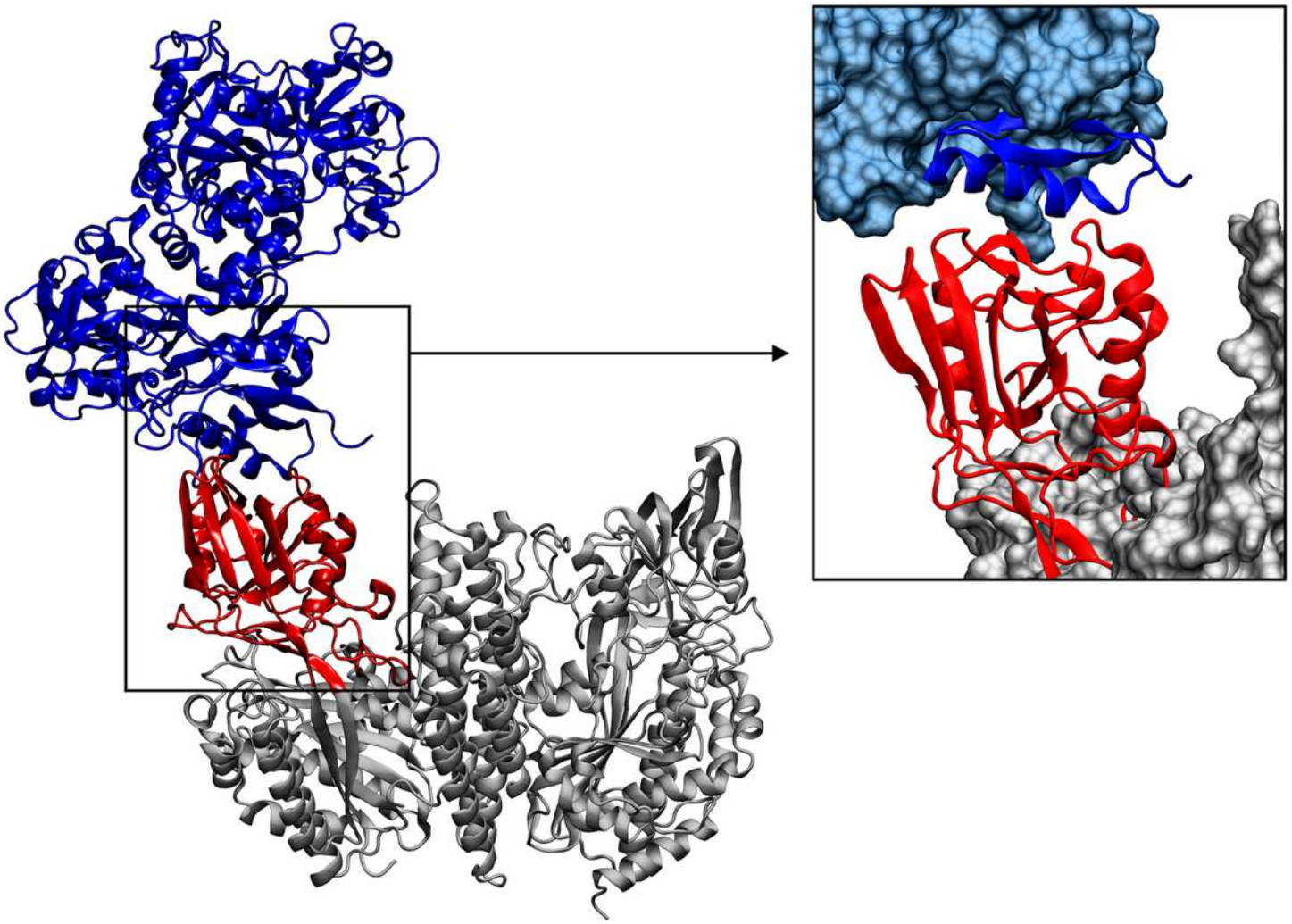

Figure 8

Complex obtained between bLf (in blue) and TfR1 (in grey). The apical domain of TfR1, binding site of bLf, is highlighted in red. A closer representation of the interaction site is shown in the right image, where the proteins are represented as a solid surface, except for the interacting regions that are shown as cartoons

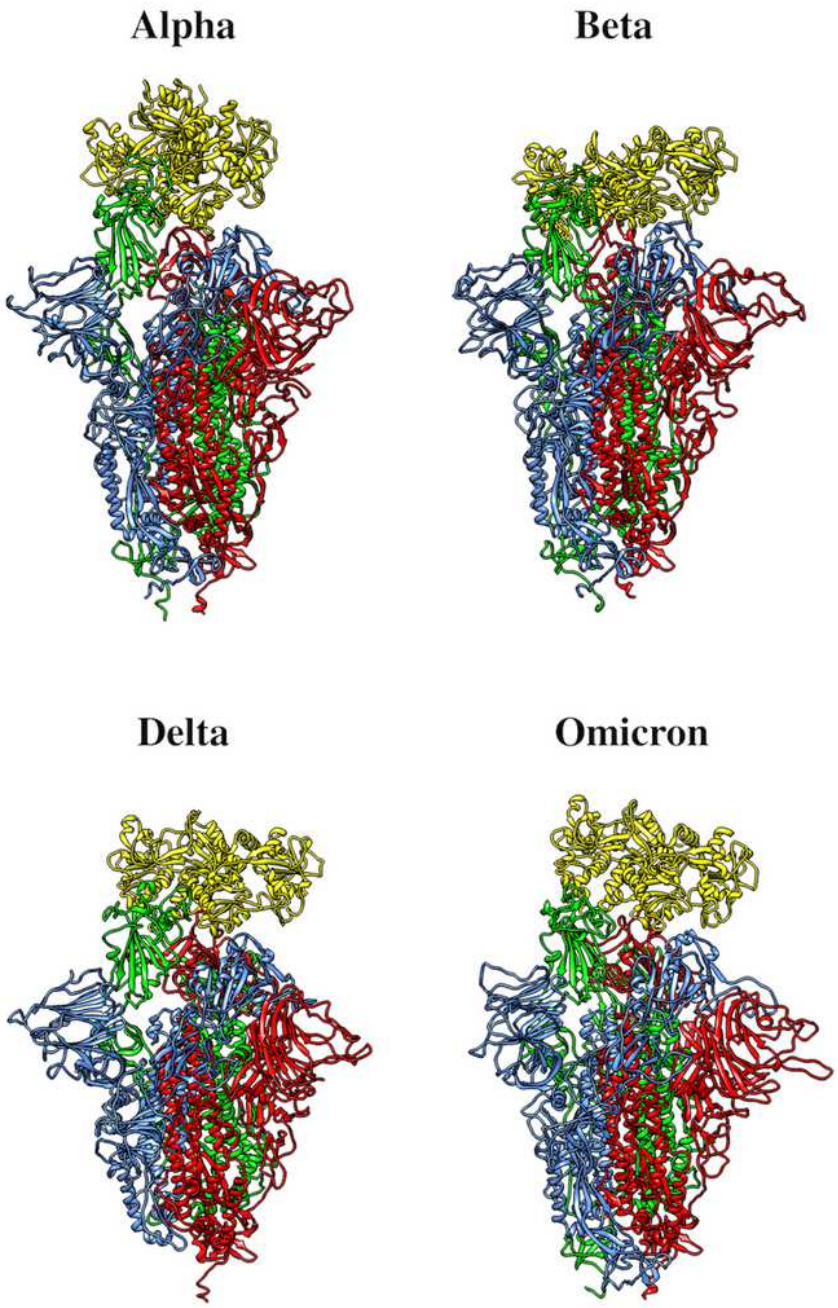

Figure 9

Complex between bLf and the four Spike variants of interest obtained through molecular docking simulations. bLf is represented with yellow ribbons, while the three different chains composing the Spike glycoprotein are represented by red, blue, and green ribbons

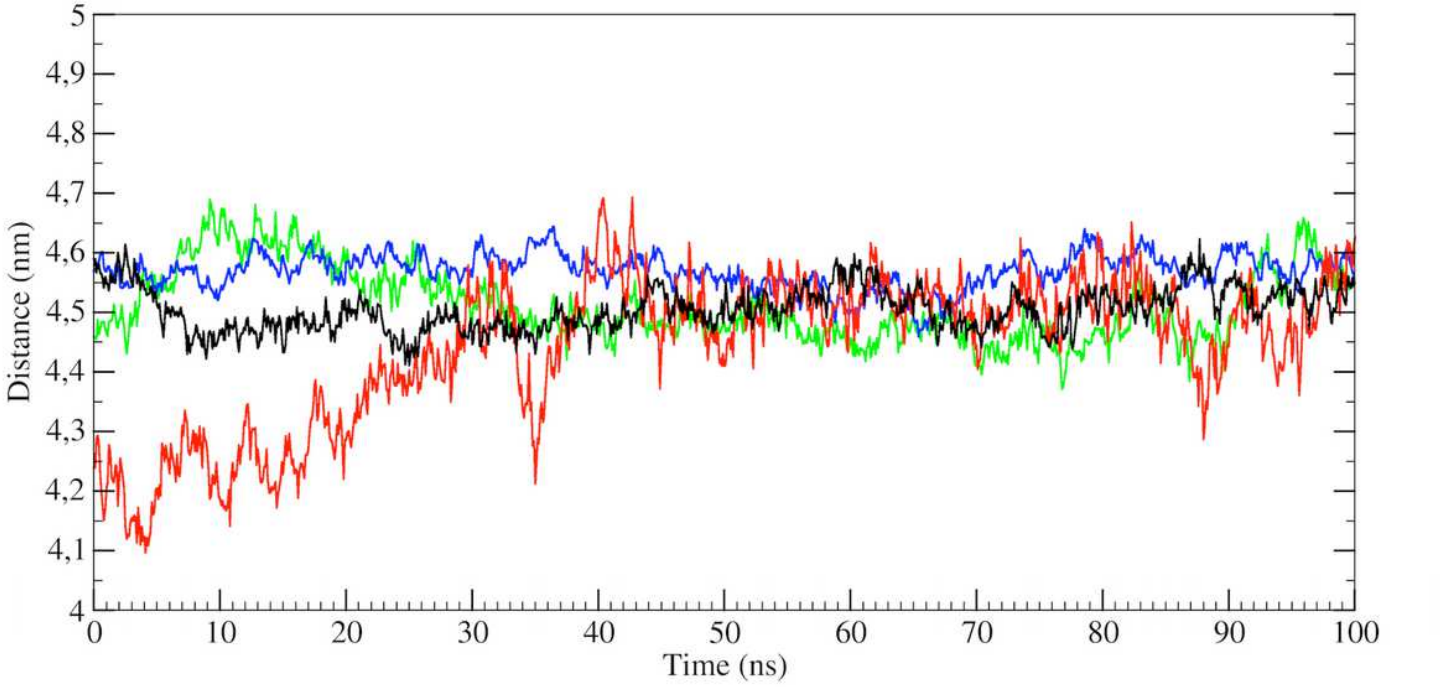

Figure 10

Time-dependent analysis of the distance evaluated between the centres of mass of the bLf and the RBD domain in the up conformation of the four Spike variants (black: Alpha, red: Beta, green: Delta and blue: Omicron)